PNNL-26213

Pacific Northwest
NATIONAL LABORATORY
Proudly Operated by Battelle Since 1965

Hybrid Gama Emission Tomography (HGET): FY16 Annual Report

February 2017

EA Miller
LE Smith
RS Wittman
LW Campbell
N Deshmukh
MA Zalavadia
MA Batie
V Mozin

U.S. DEPARTMENT OF ENERGY

Prepared for the U.S. Department of Energy
under Contract DE-AC05-76RL01830

DISCLAIMER

This report was prepared as an account of work sponsored by an agency of the United States Government. Neither the United States Government nor any agency thereof, nor Battelle Memorial Institute, nor any of their employees, makes **any warranty, express or implied, or assumes any legal liability or responsibility for the accuracy, completeness, or usefulness of any information, apparatus, product, or process disclosed, or represents that its use would not infringe privately owned rights**. Reference herein to any specific commercial product, process, or service by trade name, trademark, manufacturer, or otherwise does not necessarily constitute or imply its endorsement, recommendation, or favoring by the United States Government or any agency thereof, or Battelle Memorial Institute. The views and opinions of authors expressed herein do not necessarily state or reflect those of the United States Government or any agency thereof.

PACIFIC NORTHWEST NATIONAL LABORATORY
operated by
BATTELLE
for the
UNITED STATES DEPARTMENT OF ENERGY
under Contract DE-AC05-76RL01830

Printed in the United States of America

Available to DOE and DOE contractors from the
Office of Scientific and Technical Information,
P.O. Box 62, Oak Ridge, TN 37831-0062;
ph: (865) 576-8401
fax: (865) 576-5728
email: reports@adonis.osti.gov

Available to the public from the National Technical Information Service
5301 Shawnee Rd., Alexandria, VA 22312
ph: (800) 553-NTIS (6847)
email: orders@ntis.gov <http://www.ntis.gov/about/form.aspx>
Online ordering: http://www.ntis.gov

This document was printed on recycled paper.
(8/2010)

PNNL-26213

Hybrid Gama Emission Tomography (HGET): FY16 Annual Report

EA Miller
LE Smith
RS Wittman
LW Campbell
N Deshmukh
MA Zalavadia
MA Batie
V Mozin[1]

February 2017

Prepared for
the U.S. Department of Energy
under Contract DE-AC05-76RL01830

Pacific Northwest National Laboratory
Richland, Washington 99352

[1] Lawrence Livermore National Laboratory, Livermore, California

Executive Summary

Current International Atomic Energy Agency (IAEA) methodologies for the verification of fresh low-enriched uranium (LEU) and mixed oxide (MOX) fuel assemblies are volume-averaging methods that lack sensitivity to individual pins. Further, as fresh fuel assemblies become more and more complex (e.g., heavy gadolinium loading, high degrees of axial and radial variation in fissile concentration), the accuracy of current IAEA instruments degrades and measurement time increases. Particularly in light of the fact that no special tooling is required to remove individual pins from modern fuel assemblies, the IAEA needs new capabilities for the verification of unirradiated (i.e., fresh LEU and MOX) assemblies to ensure that fissile material has not been diverted. Passive gamma emission tomography has demonstrated potential to provide pin-level verification of spent fuel, but gamma-ray emission rates from unirradiated fuel emissions are significantly lower, precluding purely passive tomography methods. The work presented here introduces the concept of Hybrid Gamma Emission Tomography (HGET) for verification of unirradiated fuels, in which a neutron source is used to actively interrogate the fuel assembly and the resulting gamma-ray emissions are imaged using tomographic methods to provide pin-level verification of fissile material concentration.

In principle, HGET holds significant promise for the IAEA use case but quantitatively assessing its potential viability requires study of several key aspects of this active interrogation method. First, neutron interrogation of unirradiated fuels produces several candidate gamma-ray signatures and identifying the most promising signature (or combination thereof) for tomographic imaging depends on many factors, not least of which is the design of the tomographer. Initial findings indicate that imaging of individual emission energies is unlikely to be feasible due to their low intensity, but that broad energy ranges may be. Delayed gamma rays from induced fission are not initially a strong signal, but build in over the course of the measurement and become significant. Prompt gamma rays from induced fission offer a higher total emission intensity than delayed gammas, and are the largest single contribution. While the imaging of gamma rays over broad energy ranges (prompt-fission or delayed-fission) precludes imaging the concentration of individual fissile isotopes (e.g., ^{235}U or ^{239}Pu in an assembly), such a method can image the total-fissile concentration.

Second, a nominal HGET instrument design should point the way to an instrument that can assay the concentration of fissile material in reasonable measurement times and with a high degree of reproducibility. For example, the neutron source and reflector geometry must be carefully chosen in order to produce a high thermal and epithermal neutron flux that preferentially induces fission in the fissile isotopes (as opposed to fast fission in the fissionable ^{238}U) with a spatial distribution that is as uniform as possible to prevent large gradients illumination across the assembly. Given the relatively weak neutron-induced gamma-ray signatures, an HGET instrument requires detector types and collimator designs that trade off spatial resolution in favor of higher collection efficiency.

Third, standard tomographic reconstruction algorithms, for example those used in nuclear medicine and spent-fuel tomography, require high signal-to-noise in the raw signatures, and are hampered by the strong gradients in count rates between inner and outer pins of unirradiated fuel. Since the HGET use case involves relatively weak signatures and high gradients across the assembly due in large part to the coupling of neutron and gamma-ray self-shielding, there is a need to develop new reconstruction algorithms specific to HGET and the ultimate goal of IAEA measurements (i.e., confirmation of an operator's declaration about

the assembly, as opposed to assay of the assembly as a completely unknown object). The project team has preliminarily investigated a range of new algorithms that incorporate declared assembly information to account for both emission and attenuation properties, but more work is needed to quantitatively characterize their potential. Algorithms such as these can be used to verify a declaration, or as part of an iterative process starting with a simple model-independent tomography reconstruction to verify basic assembly properties prior to incorporating them into a model.

Preliminary work was performed this year, using a PWR MOX assembly with no burnable poisons as a test case. The preliminary findings from this first year of study indicate that in this case: given a careful system design, a COTS portable neutron generator, and novel reconstruction algorithms that fully acknowledge operator-declared information about the assembly, HGET appears to have the potential to verify fissile-mass concentration, on a pin-by-pin basis, in total assay times of approximately 1-2 hours – consistent with IAEA's current concept of operations, and to provide *pin-level* uncertainties consistent with the uncertainties of the IAEA's current *assembly-level* verification instruments.

Further work is needed to refine and extend this initial feasibility finding. The first priority is to extend the test cases to include LEU, and LEU with Gd rods (burnable poison). Further refinement is needed in areas such as the continuing investigation of HGET-specific tomographic reconstruction methods that fully recognize an IAEA use case focused on detecting deviations from the operator's declaration. Also, a more detailed investigation of background source terms should be undertaken—both active and passive background terms will be present, and some will be time-varying. Perhaps most importantly, the HGET viability study needs to move into empirical space. The challenges of high-fidelity simulation for this relatively complex active interrogation approach (for which even basic cross-section data are not always available) strongly encourage proof-of-principle laboratory measurements using a representative tomographic device and objects (e.g., LEU fuel rodlets), to benchmark the predictive modeling tools and guide refinement of the nominal HGET instrument design.

Acronyms and Abbreviations

BGO	bismuth germanate
BWR	boiling water reactor
COTS	commercial off the shelf
CZT	cadmium zinc telluride
DG	delayed gamma
D-D	deuterium-deuterium reaction
D-T	deuterium-tritium reaction
DU	depleted uranium
EURATOM	European Atomic Energy Community
FBP	filtered backprojection
GET	gamma-ray emission tomography
HEU	highly enriched uranium
HGET	Hybrid Gamma Emission Tomography
IAEA	International Atomic Energy Agency
ITV	International Target Values
$LaBr_3$	lanthanum bromide
LEU	low-enriched uranium
MCNP	Monte Carlo N-Particle
MOX	mixed oxide
NaI(TI)	sodium iodide (thallium doped)
LLNL	Lawrence Livermore National Laboratory
PGET	Passive Gamma Emission Tomographer
PGNAA	Prompt Gamma Neutron Activation Analysis
PNCL	Passive Neutron Coincidence Collar
PNNL	Pacific Northwest National Laboratory
PWR	pressurized water reactor
R&D	research and development
RADSAT	Radiation Detection Scenario Analysis Toolbox
RSD	relative standard deviation
UGET	universal gamma emission tomographer
UNCL	Uranium Neutron Coincidence Collar
WSU	Washington State University

Contents

Executive Summary iii
Acronyms and Abbreviations v
1.0 Introduction 1
2.0 IAEA Use Case and Fuel Definitions 4
3.0 Candidate Signatures 7
3.1 Passive Gamma Emission 7
3.2 Neutron-induced Signatures 8
3.2.1 Prompt Fission Gammas 8
3.2.2 Delayed Fission Gamma 9
3.2.3 Prompt Neutron Capture Gammas 11
3.2.4 Activation Gammas 12
3.3 Candidate Signatures: Summary and Prioritization 12
4.0 Modeling Methods and Validation 14
4.1 MCNP for Delayed Fission Gamma Rays 15
4.2 MCNP and Deterministic for Prompt Fission Gamma Rays 16
4.3 Validation of Neutron Transport Calculations 17
5.0 HGET v1 Design Study 20
5.1 Moderator/Reflector Design Variants 20
5.2 Collimator/detector study 24
6.0 Reconstruction Algorithms 28
6.1 Filtered Backprojection 28
6.2 Model-based reconstruction 28
6.2.1 Bootstrap Method 30
6.2.2 Attenuation Map vs. Activity Map, and Joint Solutions 31
6.2.3 Multi-Configuration Analysis 33
6.2.4 Pattern Matching for Missing Pins 35
7.0 Preliminary Performance Predictions 37
7.1 Case Study 1: No Pu isotopic information 38
7.2 Case Study 2: Inclusion of Pu isotopic information 41
8.0 Summary and Next Steps 44
9.0 References 47
Appendix A Emission Tomography Test Bed A.1

Figures

Figure 1. Depiction of emission tomography instrument to measure fuel emissions on a pin-by-pin basis. Hybrid gamma emission tomography (HGET) may extend this technique to fresh fuel, through the use of a neutron generator and reflector (not pictured). 2

Figure 2. PWR MOX assembly design of the 17x17—24 type with assembly averaged plutonium concentration of 7.2 wt% Pu. (From [9]) 6

Figure 3. Results of the interrogation time pattern studies for the HGETv1a instrument and MOXA fuel assembly. Emission rates as a function of the interrogation periods over the total 1 hour activation/detection time: integrated in broad energy regions (left), individual delayed gamma-ray lines (right) 10

Figure 4. Instantaneous delayed gamma emission rate, in gammas per pin per cm per s, as a function of time under constant neutron illumination. For most bins, signal continues to increase over the course of the measurement 11

Figure 5. Schematic of the HGET modeling approach. 14

Figure 6. Schematic of LLNL's approach for modeling the delayed gamma-ray response for HGET. 15

Figure 7. Schematic of PNNL's approach for modeling prompt fission gamma-ray signatures collected by HGET. 16

Figure 8. Prompt fission spectrum (from [10]) (red) with assumed group structure (magenta) for simulated pin photon sources based on pin fission rates. Integrated curves (green and blue) show total fission photons are preserved by group structure. 17

Figure 9. A qualitative comparison of the calculated induced thermal fission rate inside the 17x17 PWR MOXA assembly in the HGETv1a setup with a D-T source. LLNL-calculated result (left) and PNNL result (right). 18

Figure 10. Quantitative comparison of induced fission rates in the MOXA assembly, as calculated by LLNL (for evaluation of delayed-gamma signatures) and PNNL (for evaluation of prompt fission gamma signatures) using independent MCNP simulations. 19

Figure 11. Geometry of two source/moderator/reflector designs for total flux and thermal flux fraction for assay of a 17x17 PWR assembly: HGETv1a (left) and HGETv1b (right). 21

Figure 12. Relative thermal fission rate for HGETv1a (left) and HGETv1b (right). Each square represents one of the pins in the MOXA assembly definition. 21

Figure 13. Total cumulative fission rate with axial assembly distance. 22

Figure 14. Comparison of fissions due to low-energy neutrons, for HGETv1a and HGETv1b designs, assuming different source-plug designs. The radius of the plug (r) and length of the plug (L) are varied for the two designs. 22

Figure 15. Performance of including HGETv1a and HGETv1b for MOX and LEU fuels, for various plug variants. Results are shown for both a typical D-T (3×10^8 n/s) and D-D (3×10^6 n/s) neutron generator source. 23

Figure 16. Rendering of the PGET instrument design including the housing and fuel assembly in the interrogation chamber (left), and vertical view of the detector heads containing 104 CdTe detectors in each head (right) [3]. 24

Figure 17. Left: Variants (bottom left) on HGET collimator designs (new) compared with existing PGET (old). Bottom right: quadrature angles defined on Cartesian grid for HGET

collimator (bottom right). Resolution and intensity performance is highest for detector face at 22 cm. 25

Figure 18. Qualitative comparison of collimator effects on spatial resolution using the sinograms from PGET and HGET variants with two different radial distances (22cm and 27 cm). 25

Figure 19. Detector response for prompt fission gammas for two BGO crystals behind a center-collimator slit. Integrated counts per second (CPS) are for E > 0.5 MeV. 26

Figure 20. Reconstructed pin scores as a function of radial distance, using filtered backprojection (left), and a well-matched model-based reconstruction (right). Key assumptions: PGET instrument design, 1001 keV line for LEU, total assay time of 1 year. 30

Figure 21. Illustration of bootstrap method for including potential missing pins in a model-based pin-activity reconstruction process: Step 1 where all pins assumed present (left); 5 of the 11 missing pins are significantly different and can be identified as missing. Step 2 where five pins assumed missing based on outliers in Step 1; Step 3 where three more pins are assumed missing (total of 8) based on outliers in Step 2. 31

Figure 22. Independent reconstruction of activity with flat attenuation and attenuation with flat activity (left). The error reduction obtained (purple) for a combined score (right); missing pins are indicated by an outer diamond around the symbol. 32

Figure 23. Simultaneous reconstruction of activity and attenuation. Results are shown prior to iteration (black triangles?), and after 1 (green), 2 (red, with error bars), and 4 (black triangles) iterations. 33

Figure 24. Overview of HGET performance-prediction methodology (assuming a PWR MOX assembly) that begins with forward calculations of induced fission rate (upper left) and culminates in quantification of fissile Pu concentration in each pin. 38

Figure 25. Fission-rate integrals for ^{238}U, ^{239}Pu and ^{241}Pu, for each pin in MOXA, as function of distance from the D-T source. 39

Figure 26. Initial results for the determination of Fissile Pu (^{239}Pu + ^{241}Pu) fraction using HGET for MOXA (left) and MOXB (right). Calculated values are based on 2-hour total assay time; one-sigma error bars on statistical uncertainty are shown. Dashed lines are the actual fissile fraction (^{239}Pu + ^{241}Pu) for the three Pu loading levels. (Note that Pu isotopics are identical for all loading levels within each assembly.) 40

Figure 27. Top: fission-rate integrals for ^{238}U, ^{239}Pu, ^{240}Pu, ^{241}Pu and ^{242}Pu, for each pin in MOXA, as function of distance from the D-T source. Bottom: Initial results for the determination of Fissile Pu (^{239}Pu + ^{241}Pu) fraction in MOXA, when the incorporating Pu isotopics data in the analysis process. Calculated values are based on 2-hour total assay time; one-sigma error bars on statistical uncertainty are shown. Dashed lines are the actual fissile fraction (^{239}Pu + ^{241}Pu) for the three Pu loading levels. (Note that Pu isotopics are identical for all loading levels). 42

Figure 28. Initial results for the determination of Fissile Pu (^{239}Pu + ^{241}Pu) fraction in MOXB, using the fission integrals from MOXA. Calculated values are based on 2-hour total assay time; one-sigma error bars on statistical uncertainty are shown. Dashed lines are the actual fissile fraction (^{239}Pu + ^{241}Pu) for the three Pu loading levels. (Note that Pu isotopics are identical for all loading levels). 43

Tables

Table 1. Initial composition (before decay) of the fuel assembly definitions used in the HGET viability study (atom fractions displayed are 3x the total atom fraction, such that the U/Pu isotopes add to approximately 1). 5

Table 2. Intensity of prompt fission gamma signatures for energy windows up to 8 MeV in MOX A. 8

Table 3. Order of magnitude estimates for signal intensities from passive tomography of PWR spent fuel variants (top three entries) and HGET for unirradiated MOX fuel. HGET signatures highlighted in gray are the most promising in terms of absolute emission intensity..... 13

1.0 Introduction

Current IAEA methodologies for the verification of fresh LEU assemblies at fuel fabrication facilities utilize active neutron interrogation with neutron coincidence counting; verification of fresh MOX fuel utilizes passive neutron coincidence counting with gamma-ray spectroscopy for Pu isotopics. These volume-averaging methods are not capable of individual-pin sensitivity and as fuel assemblies become more and more complex (e.g., heavy gadolinium loading, and axial variation in boiling water reactors [BWRs]), their accuracy degrades and measurement times increase. Particularly in light of the fact that no special tooling is required to remove individual pins from modern fuel assemblies, the IAEA needs new capabilities for the verification of unirradiated fuel assemblies that can provide high-precision fissile-mass quantification, ideally at the single-pin level. The IAEA has documented the need for new unirradiated-fuel verification tools in the IAEA Department of Safeguards Long-Term R&D Plan [1]. Other potential users of a new fuel verification tools include EURATOM, and State regulators.

Passive gamma-ray emission tomography (GET) is a promising candidate for verification of item integrity in fuel assemblies because it has the potential to directly image the spatial distribution of the active fuel material, without the need for operator-declared information [2]. In this sense, it is an absolute, rather than comparative verification method. In addition, the relative intensity of gamma-ray signatures can be used to verify declared attributes on a pin-by-pin basis (e.g., burnup in irradiated fuels; uranium enrichment or plutonium isotopics in unirradiated fuels). The viability of GET for the detection of missing pins in irradiated fuels, where relatively intense, higher-energy gamma emissions are available, appears promising based on findings of a recent IAEA study [3].

For unirradiated fuels with relatively weak and lower-energy emissions, the ability to see interior pins with purely passive tomography is less clear. The use of active neutron interrogation to stimulate gamma-ray emission can provide additional signal intensity for emission tomography, here referred to as Hybrid Gamma Emission Tomography (HGET). There are several candidate signatures for hybrid (i.e., tomographic imaging of an active interrogation signature) assay of unirradiated fuels, including:

- passive characteristic gamma rays (e.g., 1001 keV from the ^{238}U daughter, ^{234m}Pa);
- prompt capture gamma rays in the isotopes of interest (e.g., 1.28 MeV from ^{235}U);
- prompt fission gamma rays (continuum peaked at ~ 1 MeV);
- delayed gamma rays from short-lived fission products (discrete lines generally from 1 to 7 MeV).

Each of the candidate signatures above has been studied previously, and sometimes in combination, for the assay of both irradiated and unirradiated fuels. For example, delayed-gamma (DG) methods have been studied for the direct assay of fissile isotopes in irradiated fuels [4, 5], but the DG methods studied to date provide no spatial information about the origin of the signatures and therefore, localized neutron moderation effects and self-attenuation can produce biases in fissile isotope quantification. In addition, the high passive background in spent fuel forces the use of only the higher-energy (> 3 MeV) DG signatures, while the most intense DG signatures are presented at lower energies. In unirradiated fuels, these more-intense, lower-energy DG signatures are accessible, but information about their location of origin in the fuel assembly is needed.

To the HGET team's knowledge, no prior work has demonstrated the ability to provide spatial information about the origin of the candidate HGET signatures and therefore, verify fuel characteristics at the pin level. In the HGET concept, it is postulated that the collection of these candidate signatures through a tomographic lens will support pin-by-pin verification of fissile materials in the assembly.

The HGET technique could be implemented in a manner similar to that used today for the assay of unirradiated LEU and MOX fuels using neutron coincidence collars. The fuel assembly would be removed from the shipping/storage container and positioned in the tomographic collar (horseshoe designs may also be possible to ease fuel handling), similar to the assembly for passive measurement depicted in Figure 1. HGET has the potential to verify: a) presence/absence of pins; b) concentration and spatial distribution of U and Pu isotopes across the assembly, and c) total U and Pu (when coupled to an active-length measurement).

In the notional HGET instrument design, multi-detector array(s) of medium-resolution gamma-ray spectrometers are positioned behind specially designed tomographic collimators. Actively induced (via a neutron generator) gamma-ray signatures are collected over the angular projections (rotation or translation of the detector arrays may be necessary) required for tomographic reconstruction. Following collection of all projection data over the entire energy range of interest, the fissile-isotope concentrations in a 2-D tomographic image of the fuel assembly are reconstructed. Tomographic reconstruction of the data will enable the user to verify the integrity of the fuel assembly on a pin-by-pin basis, in terms of total-fissile concentration and potentially, fissile-isotopic concentrations as well. Total fissile mass in the assemblies could be determined by merging tomographic data at multiple axial locations with active-length verification methods (e.g., handheld gamma scan typical of today's IAEA verification practices).

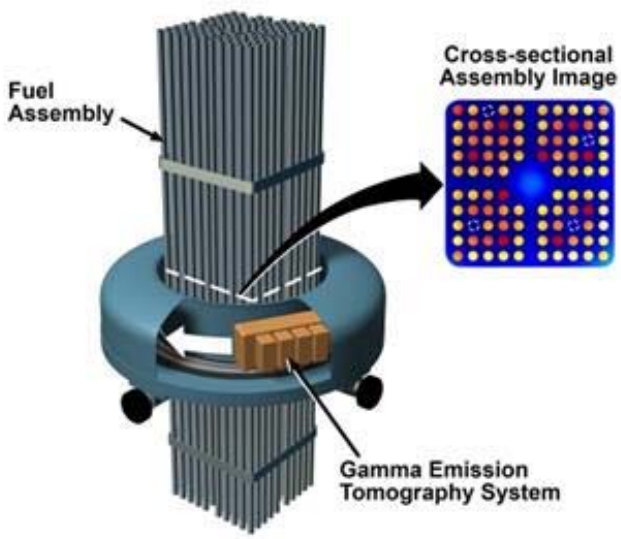

Figure 1. Depiction of emission tomography instrument to measure fuel emissions on a pin-by-pin basis. Hybrid gamma emission tomography (HGET) may extend this technique to fresh fuel, through the use of a neutron generator and reflector (not pictured).

Assessing the feasibility of hybrid gamma emission tomography for fresh fuel assay requires addressing several key questions:

- What are the most promising signatures or combinations of signatures for fissile-material assay using neutron-induced gamma-ray emission imaging?
- What are the possible source/moderator/reflector configurations that can support high-fidelity verification of fissile content in unirradiated assemblies?
- For the envisioned IAEA verification scenario, what data analysis methods (e.g. tomographic reconstruction algorithms) are capable of supporting fissile-material quantification at the pin level?
- What is the predicted performance for candidate HGET designs, in the context of the IAEA's current instruments for verification of fresh LEU and MOX assemblies?

In this project, PNNL and LLNL have built from the modeling and analysis framework, hardware design experience and analysis software developed during the IAEA SP-1 (JNT 1955) on the Viability of Gamma Emission Tomography [3]. While the UGET project provides a strong technical and collaborative foundation, the assay of spent fuel is a very different challenge than the verification of unirradiated fuels in this HGET project. For example, a key consideration is the adaptation of collimator and detector designs to recognize the very different emission energies and much lower intensities for the candidate gamma-ray signals from unirradiated fuels. The collimator and scanning protocol must strike a balance between spatial resolution and collection efficiency in order to faithfully image individual pins and achieve reasonable assay times. Detector materials and geometries should ideally provide sufficient peak-to-total efficiency (perhaps up to 10 MeV) and energy resolution to efficiently and effectively support isotopic analysis on a pin-by-pin basis. The HGET design will leverage advancements in tomography hardware components and open-source software in the nuclear medicine industry, and seek to balance performance with implementation issues that include operator impact, maintainability, and lifecycle cost. The fact that fresh/MOX fuel assemblies can be assayed in air, and the much-reduced background compared to spent fuel, means that a small-footprint, mobile instrument may be possible.

The first year of the HGET project was focused on the following topics, a list that also reflects the organization of this FY16 annual report: preliminary definition of IAEA use case and representative fuel assemblies; quantitative assessment of candidate signatures; HGET modeling framework and its validation; nominal HGET v1 design; development of HGET-specific tomographic reconstruction methods that fully incorporate declared information; simulated-based prediction of HGET performance in a notional IAEA use case involving MOX fuel assemblies. Next steps and planned HGET activities in FY17 are also discussed.

2.0 IAEA Use Case and Fuel Definitions

The use case for an HGET instrument is presumed to be consistent with how current IAEA instrumentation is used for the verification of unirradiated fuels. For fresh LEU fuel, the IAEA uses the Uranium Neutron Coincidence Collar (UNCL); for MOX fuel the Passive Neutron Coincidence Collar (PNCL). Both instruments use neutron coincidence signatures to verify the total uranium or plutonium in the assembly--additional information about each method is given below [6], along with IAEA's International Target Values (ITVs) [7] for verification of unirradiated assemblies.

For fresh LEU fuel, the UNCL is used to measure the mass density of ^{235}U at a given axial location of the assembly. It is assumed that the ^{235}U is the only fissile isotope in the assembly and therefore, that all induced fission comes from ^{235}U. This localized ^{235}U mass density is translated to total ^{235}U mass for the assembly using an active length measurement (e.g., gamma scanning). The ITV for determination of total ^{235}U mass in an LEU assembly is 4.5% (one-sigma relative), assuming relatively low gadolinium content. Count times are not specified in the ITV document, but information provided by other sources indicate that measurement times for UNCL, on fuels with relatively low Gd concentration, are approximately one hour to reach the desired statistical uncertainty. Systematic uncertainties for high-Gd assemblies can be 10 or more times higher.

For MOX fuel, the PNCL is used to measure the mass density, at a given axial location, of the Pu isotopes with appreciable spontaneous fission yields (^{240}Pu dominates). High-resolution gamma-ray spectroscopy on exterior pins of the assembly is then used to infer the linear density of total Pu. An active length measurement (e.g., gamma scanning) is employed to translate that value to total Pu for the assembly. The ITV for determination of total Pu mass in a MOX assembly is 3.2% (one-sigma relative). Count times are not specified in the ITV document, but information provided by other sources indicates that measurement times are typically on the order of 15 minutes.

The use cases and ITVs for UNCL and PNCL provide useful context for the HGET viability study. For example, the following assumptions were made to guide the HGET study:

- Verification of unirradiated fuel will occur in an air environment and the operator will position the fuel assembly in such a way that the HGET collar will assay one or more vertical segments of the assembly. As with UNCL and PNCL, it is assumed that some form of active-length measurement will inform the translation from the HGET-measured ^{235}U and total Pu linear densities to a ^{235}U and total Pu assembly mass value. Note that the HGET gamma-spectrometer array, operating in purely passive mode, could provide an active-length measurement similar to what is performed today using a handheld gamma-ray detector. (This assumes that the operator moves the fuel assembly through the HGET collar.)

- Total measurement time for HGET verification of unirradiated fuel assemblies should be on the order of 1-2 hours. While today's measurements may be shorter in duration, the fact that HGET will provide pin-by-pin verification of fissile content encourages a broader window of assay-time acceptability for the first phase of the study.

- The physical dimensions and mass of HGET should be comparable to existing IAEA instruments: for example, the JCC-71 PNCL/UNCL instrument sold by Canberra weighs approximately 40kg [8]. A maximum neutron moderator/reflector weight of 100 kg was enforced during the design study, on

the logic that this represented a reasonable size for a mobile instrument deployed at a fuel fabrication or reactor facility.

To support the simulation-based HGET design and viability study, nominal fuel assemblies—both LEU and MOX—were defined. For the MOX, the age since separation for the reactor-grade Pu was assumed to be 5 years, an upper limit in terms of occupational health hazards (after about 5 years enough ^{241}Am has grown in to make handling difficult; this process has little impact on the amount of fissionable material for the HGET measurement). The composition of the fuel-assembly definitions used for the FY16 HGET study, dubbed MOX Composition A (MOXA), MOX composition B (MOXB), and LEU, are shown in Table 1. In this initial study, we focus on a PWR assembly with 17x17 pins. PWR fuel is at the more-challenging end of the continuum of fuel types under safeguards in terms of neutron and gamma-ray attenuation, due to its relatively dense pin-array geometry and overall large dimension. VVER-1000 would be even more challenging, while BWR would be significantly less difficult. Other fuel types will be considered in future work.

Table 1. Initial composition (before decay) of the fuel assembly definitions used in the HGET viability study (atom fractions displayed are 3x the total atom fraction, such that the U/Pu isotopes add to approximately 1).

		MOXA	MOXB	LEU
Atom	Isotope	Atom Fraction (X3)	Atom Fraction (X3)	Atom Fraction (X3)
U	234	5.20×10^{-5}	5.20×10^{-5}	3.12×10^{-3}
U	235	6.81×10^{-4}	6.81×10^{-4}	4.05×10^{-2}
U	238	9.39×10^{-1}	9.39×10^{-1}	9.60×10^{-1}
Pu	238	1.36×10^{-3}	7.75×10^{-4}	
Pu	239	3.21×10^{-3}	2.75×10^{-2}	
Pu	240	1.52×10^{-2}	2.03×10^{-2}	
Pu	241	7.06×10^{-3}	6.25×10^{-3}	
Pu	242	4.21×10^{-3}	5.17×10^{-3}	
O	16	2	2	2
	density (g/cc)	10.4538	10.4538	10.4538

Generally speaking, the composition of MOX fuel pins varies with pin position. The IAEA technical report, Status and Advances in MOX Fuel Technology, gives Pu concentrations of each pin type in an example MOX assembly, as shown in Figure 2 [9]. Note that the overall Pu concentration varies from pin to pin but the relative Pu isotopics, as defined in Table 1, is consistent across all pins.

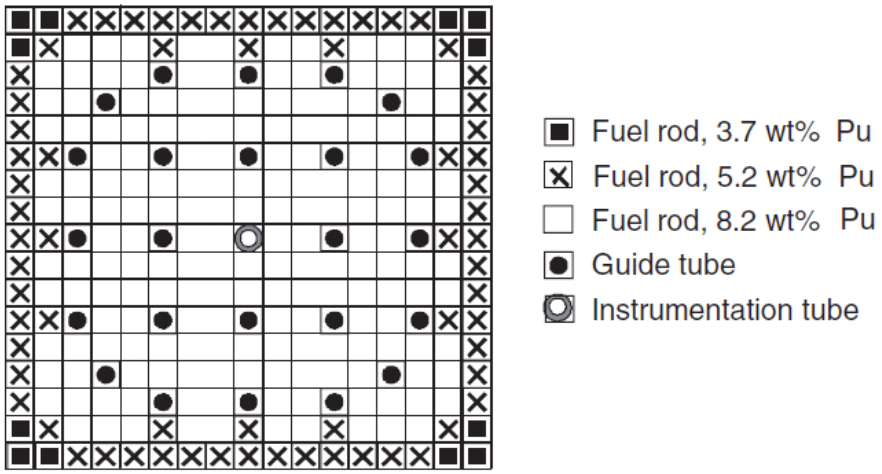

Figure 2. PWR MOX assembly design of the 17x17—24 type with assembly averaged plutonium concentration of 7.2 wt% Pu. (From [9])

3.0 Candidate Signatures

Gamma emission tomography is based on detecting gamma emissions selectively, sensitive to both their location and their angle of incidence. This requires high-intensity emissions in order to achieve high confidence in reasonable assay times; as spatial resolution becomes finer even higher emission rates are needed to maintain a certain signal to noise level, given a fixed assay time. In order to measure the inner fuel pins, radiation from these pins must pass through a considerable distance of very dense, very high Z material. Attenuation of the inner-pin signal can make the detection of inner pins very difficult, given practical constraints on the size and complexity of fuel interrogation instruments, and particularly if relatively short assay times are required. Gamma rays with energies of less than 500 keV have a very low probability of escaping from inner pins to the outside. Penetration increases with increasing energy to a maximum at around 3 MeV to 4 MeV, beyond which the pair production mechanism of absorption causes penetration to decrease. The penetration maximum is fairly broad, however, such that gamma rays with energies of 1 MeV and above are roughly comparable in terms of penetration ability. Isotopic specificity is also desirable; if a gamma-ray emission is uniquely tied to a given isotope (e.g., fissile isotope or fission product), it will likely be more useful in characterizing the fissile content of the assembly. Finally, methods based on excessively complex signatures may be difficult to implement, limiting their utility. Discussion of the various candidate HGET signatures considered in FY16 is given below.

3.1 Passive Gamma Emission

For spent fuel assemblies, large amounts of fission products are present, producing abundant gamma radiation for imaging. The ability to image based on individual gamma spectral lines from fission products can be used to quantify fuel burnup and indicate pin presence (see [3]), but does not directly assay fissionable material. The most important lines for spent fuel with relatively short (i.e., 1-5 years) cooling time are the ^{154}Eu lines at 723, 873, 996, 1005, and 1274 keV. For a PWR assembly at 20 MWd/MTU burnup and 1 year cooling time, the line-specific activity at 1274 keV is 1.4 x 10^8 γ/pin/cm/s; at 5 years cooling time this number is reduced to 1.0 x 10^8 γ/pin/cm/s. These count rates are observed to be high enough to allow pin-level emission imaging on a timescale of 1 hour or less [3]. For spent fuel with a longer cooling time, the ^{137}Cs line at 662 keV has sufficient intensity for imaging, but the lower energy results in decreased ability to resolve the innermost pins of a large assembly; the same PWR assembly at 30 years cooling time has a ^{137}Cs line-specific activity of 4.8 x 10^9 γ/pin/cm/s [3]. Although the count rate due to ^{154}Eu is lower than due to ^{137}Cs at all cooling times, at shorter cooling times when sufficient counts are available, the ^{154}Eu is the better discriminator of missing pins due to the increased penetration of the higher energy gamma lines. Though spent fuel is not the focus of the HGET study, the approximate emission intensities of key signatures is given here as context for the intensity of the candidate HGET signatures.

Fresh fuel also emits passive gammas, most notably the ^{234m}Pa 1001 keV line (for LEU) and the ^{239}Pu 414 keV line (for MOX). ^{234m}Pa is part of the ^{238}U decay chain, and comes into secular equilibrium with ^{238}U approximately a month after processing, at which time it becomes an indicator of ^{238}U abundance. Simulations of a MOX fuel assembly (MOXA, described in Section 2) indicate a 1001 keV line-specific activity of 343 γ/pin/cm/s. The 414 keV line of ^{239}Pu provides a direct signature for the presence of plutonium, but is not very penetrating, making it very difficult to image interior pins. Simulations of the same MOX assembly indicate a 414 keV line-specific activity of 5282 γ/pin/cm/s.

3.2 Neutron-induced Signatures

The passive emissions from unirradiated LEU and MOX fuels are many orders of magnitude less than from spent fuel. Emission tomography based on these lines would require greatly increased measurement times and likely decreased spatial resolution, making them impractical for assay. Current methods for fresh fuel assay also include neutron interrogation – the UNCL uses a neutron source to stimulate fission, and detect coincident fission neutrons. In addition to fission neutrons, a fuel assembly under neutron interrogation will emit gamma radiation originating from multiple interactions: prompt-fission gammas, delayed fission gammas, prompt-capture gammas, and activation.

The count rates below are modeled using methods described in Section 4. We assume a commercial, off-the-shelf neutron generator which is small enough to transport (Thermo Scientific P 385), using a deuterium-tritium reaction (D-T) to produce approximately 10^8 n/s at 14.1 MeV. The neutron environment is also described in Section 4; feasibility calculations were done for the instrument configuration labeled HGETv1a, as described in Section 5. For fuel, the estimates below assume the MOX composition labeled "MOXA" and described in Section 2.

3.2.1 Prompt Fission Gammas

Prompt fission gammas come from the fission stimulated by active neutron interrogation; on average, approximately 3 photons per fission. Verbinski *et al.* [10] show that the resulting fission photon spectrum is largely insensitive to the isotopic species undergoing fission, producing a plateau from low energies (<0.1 MeV) to about 0.7 MeV, beyond which the spectral intensity falls off quickly.

Modeled data for a MOXA assembly and a 10^8 n/s D-T source yields 5965 fissions/pin/cm/s averaged over all pins. Taking the fission spectrum from Verbinski *et al.*, the fission gamma-ray spectrum can be estimated. Dividing the spectrum into 0.5 MeV bins gives the production rates shown in Table 2. Excluding gamma rays with energy less than 0.5 MeV as insufficiently penetrating, the estimated emission rate for prompt fission gamma rays suitable for imaging unirradiated fuel is approximately 27,000 γ/pin/cm/s. If only the highly penetrating gamma rays above 1 MeV are considered, the rate is approximately 13,000 γ/pin/cm/s.

Table 2. Intensity of prompt fission gamma signatures for energy windows up to 8 MeV in MOX A.

Energy Window		Fission Gamma Intensity
Low (MeV)	High (MeV)	γ/pin/cm/s
0	0.5	18639
0.5	1	13992
1	1.5	5976.4
1.5	2	2735.1
2	2.5	1620.2
2.5	3	1055.5
3	3.5	629.8
3.5	4	413.7
4	4.5	257.5

Energy Window		Fission Gamma Intensity
4.5	5	167.1
5	5.5	98.0
5.5	6	59.3
6	6.5	37.1
6.5	7	22.3
7	7.5	10.6
7.5	8	4.6

The prompt fission gamma rays provide evidence of fissile material, although fast fission of ^{238}U also contributes to the signal. Prompt fission gamma signatures cannot provide isotopic or elemental characterization of the assembly's composition. If assumptions are made about the assembly composition, either through operator declaration or the use of other spectroscopic signatures, the amount of ^{235}U or fissile plutonium in in each pin can be verified using prompt fission gamma rays.

A difficulty may arise in that prompt fission gamma rays must be measured while the interrogating neutron generator is active. This raises concerns about neutron interaction in the detector. Additional design features may be needed to ensure that the gamma detector is sufficiently shielded from neutrons, or that the detector material is not highly sensitive to neutrons.

3.2.2 Delayed Fission Gamma

Delayed gamma methods have been studied for the direct assay of fissile isotopes in irradiated fuels [4, 5]. Fission is stimulated with an interrogating neutron source, and the discrete lines from the decay of short-lived fission products are measured. The measured gamma spectra can then be fit to a linear combination of spectra from pure ^{239}Pu, ^{241}Pu, and ^{235}U to determine the proportion of fissile isotopes present. Because a variety of short-lived isotopes are produced, the lines emitted from the fuel assembly will vary significantly over time. To focus on short-lived isotopes, particularly for a tomography measurement which will require minutes or hours to complete, pulsing the neutron generator and measuring the response after the pulse is required.

A modeling effort was dedicated to the investigation of the interrogation time structure and the energy distribution of the induced delayed gamma-ray signal in the HGETv1a setup. Such analysis requires well-sampled statistics in the high-resolution response spectrum, and is generally achievable with high-efficiency spectroscopy systems or over long dwell times. In addition, the interrogation time pattern can affect the production of individual gamma-ray lines, depending on the half-life of the parent fission product. The ability to distinguish individual gamma-ray peaks from the short-lived fission products is critical if quantification of individual fissile isotopes is needed, but not essential for assay of total fissile material.

Timing effects were investigated for measurement periods of up to one hour, to be consistent with operational constraints. Previous work demonstrated that the 50% interrogation time pattern (activation and data collection periods have the same length) is the most favorable for spectroscopic observations of short-lived activation products [5]. To determine an appropriate extent of the activation/detection time with a D-T neutron source, the total 1 hour measurement time was divided in multiple intervals assuming the following periods: 1, 5, 10, 20, 30, 60, 300, 900, and 1800 seconds. The most extreme one-second case

assumes that the measurement is completed in a protocol that begins with a one-second activation period and is followed by a one-second detection period repeated 1800 times over an hour. On other extreme, the 30-min activation and 30-min detection are performed just once within the allotted total assay time of one hour. Modeling results for this case are demonstrated in Figure 3, both for the large regions in the detected spectrum and for the most intense individual delayed gamma-ray lines predicted for the MOXA assembly.

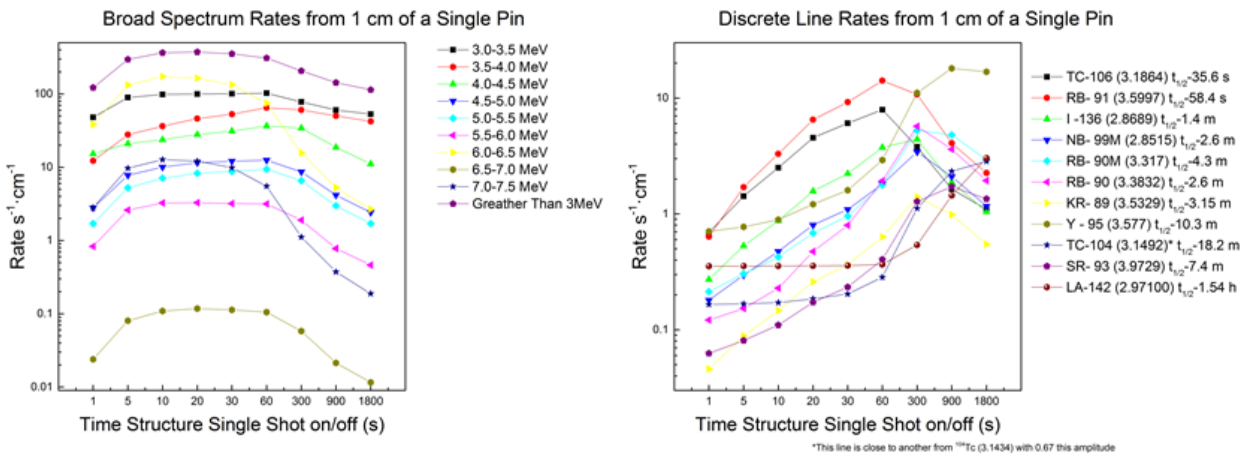

Figure 3. Results of the interrogation time pattern studies for the HGETv1a instrument and MOXA fuel assembly. Emission rates as a function of the interrogation periods over the total 1 hour activation/detection time: integrated in broad energy regions (left), individual delayed gamma-ray lines (right).

These simulations give approximately 600 γ/pin/cm/s for all delayed gamma rays with energy greater than 3 MeV. This type of broad-window data collection could support quantification of total-fissile concentration. For determining the concentration of individual fissile isotopes, specific delayed gamma lines will need to be measured and their ratios analyzed (See References [4, 5, 11-13]), but those individual line intensities range from about 20 γ/pin/cm/s to well less than 1 γ/pin/cm/s. This analysis suggests that the HGETv1 design (i.e., 3 x 10^8 n/s D-T source) will not support the individual delayed gamma-ray line spectroscopy within 1 hour of the total measurement, but that tomographic reconstruction may be possible using broad energy windows. However, for the time structures investigated here, the count rate remains low.

An additional delayed gamma calculation was investigated to understand delayed gammas when the neutron source is on constantly, rather than pulsed. It was observed that for most broad energy bins, the delayed gamma emissions will continue to increase over the course of minutes or even tens of minutes, as shown in Figure **4**. The integrated signal over 1 MeV approaches 5000 gammas/pin/cm/s after 1000 seconds of illumination.

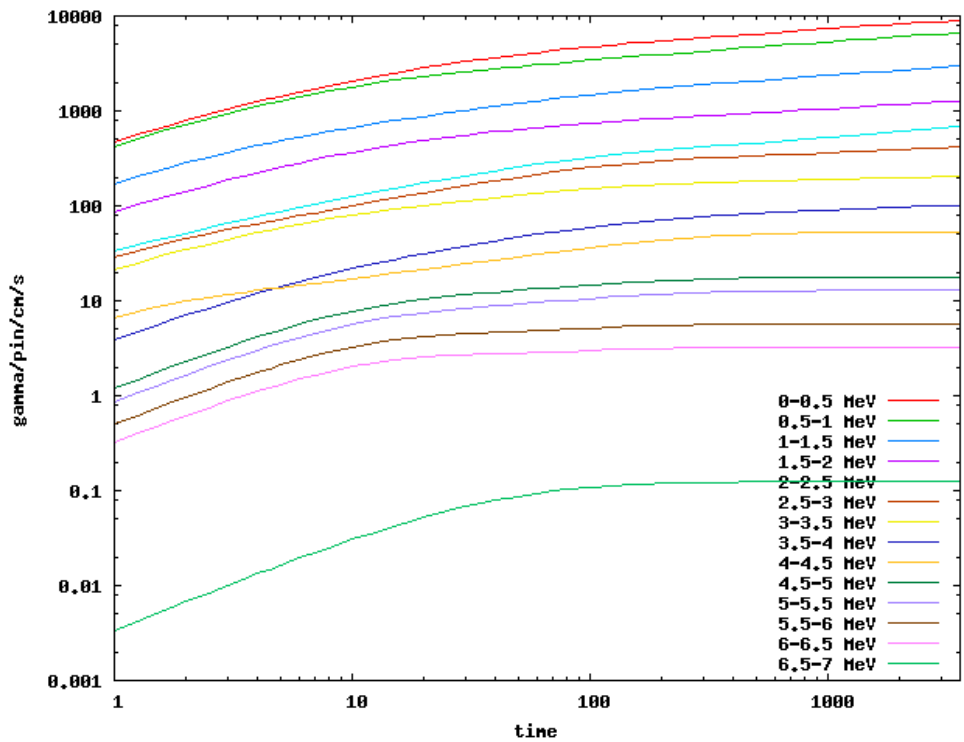

Figure 4. Instantaneous delayed gamma emission rate, in gammas per pin per cm per s, as a function of time under constant neutron illumination. For most bins, signal continues to increase over the course of the measurement.

This suggests that delayed gammas, in broad energy regions, will have a count rate which is amenable to tomography after a few minutes of illumination. However, most tomography reconstruction algorithms implicitly assume that the conditions are not changing over the course of the measurement. Incorporating a time-varying signature will require an adjustment to the reconstruction algorithm to take this into account.

3.2.3 Prompt Neutron Capture Gammas

The (n,γ) reaction offers another potential pathway for distinguishing the isotopic composition of nuclear fuel, using Prompt Gamma Neutron Activation Analysis (PGNAA). Simulations of neutron capture have not been performed, but the simulations of fission rates in the assembly can be used to provide rough estimates of the capture rates. Starting with 2861 plutonium fissions/pin/cm/s and a ^{239}Pu thermal neutron fission cross section of 751.3 barns (b), the thermal flux in the assembly can be estimated. Using the partial cross section for production of a given gamma ray [14] and the relative isotopic abundance of the capturing isotope we can estimate the capture gamma-ray production. There is enough error in the initial assumptions that these estimates will not be precise, but they should provide a guide for the potential viability of prompt capture gamma rays.

The isotope ^{238}U is roughly ten times as abundant as plutonium in the model MOXA assembly. The most significant capture line is at 4.06 MeV, with a capture cross section of 0.186 b [14]. This gives an estimate of 7 γ /pin/cm/s for the capture gamma rate. The total (n,γ) cross section is 2.69 b at thermal energies [15], although many of these gamma rays will be too low energy to be useful. This puts an upper bound of approximately 100 γ /pin/cm/s for all ^{238}U(n,γ) reactions.

The MOX assemblies used for our preliminary investigations have little ^{235}U. However, the signal of neutron capture on ^{235}U in LEU assemblies can also be considered. Assuming the fission rate under interrogation is about the same and all comes from ^{235}U, we can use the 98.8 b $^{235}\mathrm{U}(n,\gamma)$ and 585.5 b $^{235}\mathrm{U}(n,f)$ cross sections to give a maximum of 483 γ/pin/cm/s. The PGNAA databases list a partial cross section of 0.2 b for the 1.28 MeV capture gamma ray, giving about 1 γ/pin/cm/s at the most prominent line. However, the 0.2 b value might be for elemental uranium -- certainly the sum of the cross sections for all listed lines adds up to only 0.6 b, a far cry from the total (n,γ) cross section. If this is true, the isotopic capture cross section for the 1.28 MeV gamma would be 27.8 b and the rate of production would be an estimated 135 γ/pin/cm/s. At this point, there is insufficient data to indicate which estimate is the more correct.

There is little available data on the neutron capture gammas from plutonium. The (n,γ) cross section from the various isotopes is known, but not the energies or intensities of the resulting gamma rays. Assuming a composition of primarily ^{239}Pu, the capture cross section of 271.8 b allows an estimate of the upper limit of plutonium neutron capture gamma rays of 1035 γ/pin/cm/s.

The fuel material is an oxide of the actinide materials. Mapping the oxygen distribution would provide a useful determination of the presence of fuel. Unfortunately, the partial cross sections for capture gamma rays of oxygen are very small, on the order of 10^{-4} at best. Consequently, gamma rays from the capture of neutrons on oxygen will be negligibly small.

3.2.4 Activation Gammas

The activation products of fuel materials tend to be either non-radioactive (*e.g.* ^{17}O) or long lived ($t_{1/2}$ > 1 hour). The exceptions are ^{19}O and ^{239}U. The former has a low cross section for production and a low isotopic abundance of its precursor, and the latter suffers from small branching ratios for the production of energetic gamma rays upon decay. Thus, activation gamma rays do not provide attractive signals for tomography of assemblies. Even if an activation signal could be detected, it would suffer from the same difficulty as the delayed gamma emission, in that the signal would be time-varying and difficult to interpret. Even further, the candidate isotopes are only indirect indicators of the fissile material in the pin, as opposed to a direct measure.

3.3 Candidate Signatures: Summary and Prioritization

The possible signatures for hybrid gamma emission tomography for fresh fuel are listed in Table 3, with a few numbers corresponding to passive signatures for spent fuel included for comparison. Even with neutron interrogation using a D-T generator at 3×10^{8} n/s, emission rates for neutron-induced signatures in irradiated fuels are several order of magnitude lower than the key signatures present in spent fuel.

Table 3. Order of magnitude estimates for signal intensities from passive tomography of PWR spent fuel variants (top three entries) and HGET for unirradiated MOX fuel. HGET signatures highlighted in gray are the most promising in terms of absolute emission intensity.

Technique	Emission rate (γ/pin/cm/s)
Spent fuel, 1 year CT, ^{154}Eu 1274 keV	1.4×10^8
Spent fuel, 5 year CT, ^{154}Eu 1274 keV	1.0×10^8
Spent fuel, 30 year CT, ^{137}Cs 662 keV	4.8×10^9
^{234m}Pa 1001 keV (LEU)	300
^{239}Pu 414 keV (MOX)	5000
Prompt fission in MOX, > 1000 keV	13000
Delayed gamma in MOX, individual lines	< 20
Delayed gamma in MOX at 1 s, > 1000 keV Delayed gamma in MOX at 1000s, > 1000 keV	350 4700
Prompt capture gamma in MOX, U	Uncertain, ~100's
Prompt capture gamma in MOX, Pu	<1000
Activation gammas > 500 keV in MOX	Uncertain, small

Some additional interpretation and discussion of the candidate HGET signatures is provided here. There is currently insufficient data to determine if prompt neutron capture gamma rays would be useful or even detectable; if so, they could provide compositional information about fissile isotopes an assembly, at least for the outer pins. Likewise, passive gamma rays offer a potential method of assaying the ^{239}Pu in outer pins and ^{238}U over some or all of the assembly, but emission rates are low and the 414-keV photons would have difficulty reaching the detector from the interior of the assembly. Delayed gamma signatures are more complex, due to their time dependence, and no individual lines are observed with sufficiently high emission intensity for tomography. It is possible that a delayed gamma-ray signature summed over broad energy windows could be imaged – but fissile-isotope specificity would be lost. The assay of other activation products to infer fuel composition offers little promise both because of low intensity and limited direct connection to the fissile material that is the focus of IAEA verification. Given that no isotope-specific signatures are high enough in intensity for direct fissile isotope assay, the most useful signature for verifying the integrity of fuel assemblies and total fissile content appears to be the prompt fission gamma rays due to their relatively high production at energies above 1 MeV – although still four orders of magnitude below emission rates typical of spent fuel. This large gap in emission intensity points to the need for the development of HGET-specific tomographic designs and methods, for example detector and collimator designs for lower spatial resolution imaging, and tomographic reconstruction methods that incorporate *a priori* information about the pin assembly geometry; these investigations are discussed in sections 5 and 6, respectively.

4.0 Modeling Methods and Validation

Simulation has provided the foundation for the HGET viability study to date, and will continue to guide and inform the study in the future. The HGET interrogation scenario presents a complex problem for modeling: active neutron interrogation to produce gamma rays means that both neutron and gamma transport calculations are required. The delayed gamma signature is time dependent, adding additional complexity. The variations in attenuation in the problem are enormous, and the probability of a photon emitted from an inner pin reaching the detector is extremely small, making Monte Carlo transport difficult and inefficient. This difficult problem requires a flexible modeling approach, and is most efficiently tackled by breaking the problem into separate pieces, as shown in Figure 5.

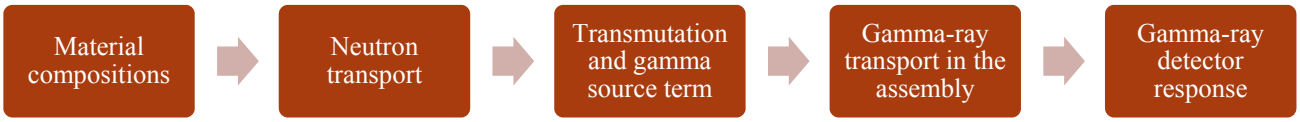

Figure 5. Schematic of the HGET modeling approach.

Material compositions are defined based on known fuel types, for example the LEU and MOX definitions described previously. The geometry and material composition definitions are used by analysts to build models for the neutron transport. In HGET, both PNNL and LLNL performed neutron transport using Monte Carlo methods. The neutron flux in each pin is used to calculate the reaction rate for the reaction of interest (e.g., fission, capture), which is then used to produce a corresponding gamma-ray source term (e.g., prompt-fission or delayed fission gamma rays). This spatially dependent gamma-ray source term drives a completely separate calculation of gamma-ray transport through the assembly. Two different methods were employed for the gamma-ray transport: Monte Carlo by LLNL and deterministic by PNNL. Monte Carlo is a standard approach for modeling radiation transport, while deterministic can be significantly faster, enabling a wide range of simulations. By using both we are able to validate that the results are consistent. Finally, the gamma-ray flux at the detector face is converted by a gamma-ray detector response. Methods for calculating detector response vary, but are either analytical or Monte Carlo in foundation. The modeling methods used for different candidate signatures are described in the sections that follow and related references.

It is important to note that the HGET modeling work to date is focused on initial, proof-of-principle performance estimation, and therefore the degree of fidelity and benchmarking differs from other undertakings. In some cases, the nuclear data (e.g., cross sections or emission yields) is simply not available to support high-fidelity, thoroughly benchmarked simulations—this is especially the case with short-lived responses for delayed gamma rays. For example, prior experimental work on delayed gamma emissions with foils has revealed a number of short lived isotopes which have cross sections inconsistent with literature values [16]. The modeling and analysis framework described in this section focuses on the delayed gamma and prompt fission gamma signatures. Important to note is that the scoping studies in FY16 assume negligible background during the collection of the prompt fission gamma and delayed gamma signatures. Further effort is needed to better understand the nature of the background during measurement of these signatures.

4.1 MCNP for Delayed Fission Gamma Rays

Modeling the delayed gamma-ray response induced in the unirradiated fuel assembly with an external neutron source was performed in support of the preliminary HGET instrument design and viability analysis by LLNL. LLNL's MCNP-based modeling of delayed gamma signatures assumed the HGETv1a configuration (See Section 5), the MOXA 17x17 PWR fresh fuel assembly coupled with a D-D or a D-T neutron source. The modeling methodology implemented at LLNL is based on a hybrid computational approach in which analytical and Monte Carlo solvers are in a sequence as illustrated in Figure 6. The primary advantage of this modular scheme, developed in earlier studies [5, 13], is the ability to split a complex calculation process into individual steps, and in particular to separate data-heavy spent fuel transmutation, the gamma-ray source definition, and the detector response reconstruction from the time-consuming 3D transport calculations. The Monte Carlo module implements modeling of neutron and gamma-ray transport in complex 3D geometries using the MCNP6 code [17]. It provides effective variance reduction solutions that enhance the computational performance in large parallelized architectures. The analytical CINDER/DGSDEF module enables fast and exact, point-kinetic calculations of material inventory evolutions, spontaneous and induced fission reaction rates, as well as passive and delayed gamma-ray source terms [18, 19].

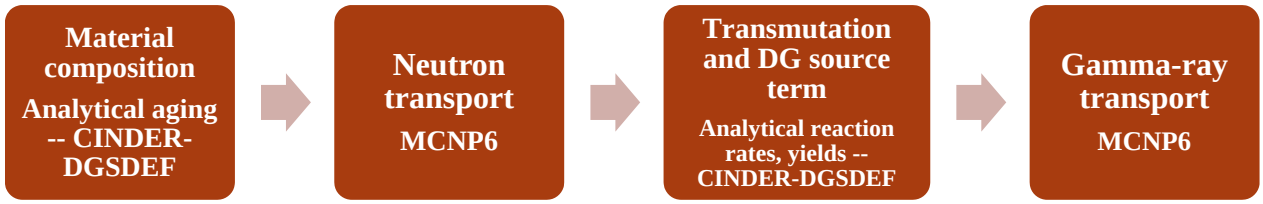

Figure 6. Schematic of LLNL's approach for modeling the delayed gamma-ray response for HGET.

The adopted approach to modeling neutron-induced delayed gamma-ray responses was benchmarked against a variety of available experimental data measured from HEU, DU, weapons grade Pu and mixed samples activated at accelerator facilities and with portable neutron sources [13]. It was also used to reproduce high-resolution passive gamma-ray spectra measured from real spent nuclear fuel assemblies measured at the Clab facility in Sweden [3]. At the first stage of the calculation, the initial fuel inventory indicated in Table 1 is aged by 5 years, by developing all possible daughter products from naturally occurring decay chains. As a result, a more complex material composition is developed for each assembly pin. At the second stage, these extended pin-specific material definitions are introduced into the 3D MCNP6 model of the assembly and the HGET measurement setup. A transport calculation for the interrogating neutron source is performed and a neutron flux in pre-defined axial regions of each assembly pin is determined in a 64-group energy structure. At the third stage, a comprehensive analytical calculation of transmutation processes is completed. Fission products are created and decay patterns are developed using an extensive dataset of 3400 nuclides with Z ranging from 1 to 103 in ground and isomeric states; 98 nuclides with spontaneous and neutron-induced fission yields (at thermal, fast, and high energy regions) for 1325 fission products. Neutron reaction cross sections, including induced fission events are defined for each region in the 64-group neutron flux energy structure. Activated material evolutions are propagated through the irradiation time patterns and the resulting inventories are used to define the gamma-ray emission source term. At the fourth stage of the process, the full 3D Monte Carlo calculation is used to propagate the gamma-ray source term defined in each individual pin to the detector component of the measurement setup.

The individual pin approach to calculating fuel material transmutations and gamma-ray source terms implemented in the four-step scheme allows for the investigation of neutron-induced effects in more detail. In particular, it provides information about the relative contributions to the total induced fission rate from each of the Pu and U isotopes present in the fresh fuel. In turn, this allows for the determination of the relative sensitivity of the measurement concept to individual SNM components of the fuel.

The initial HGET modeling studies for delayed gammas were focused on the development of the optimal activation setup configuration, determining the relative efficiency of D-D and D-T neutron sources, and on investigating the irradiation time patterns.

4.2 MCNP and Deterministic for Prompt Fission Gamma Rays

As a first step in calculating the prompt fission gamma emission rates, PNNL used MCNP to calculate the pin-specific total fission rate, in a manner very similar to the simulations performed by LLNL for modeling delayed gamma rays (previous section). Using 10^7 neutron histories, the fission rates for both fissionable and fissile isotopes were calculated to a statistical precision of less than 1% for each pin. To ensure statistical convergence for the Monte Carlo steps in the prompt-gamma modeling sequence, standard statistical measures were used for the Monte Carlo calculations. As will be described in Section 4.3, PNNL's neutron modeling was checked for consistency against the LLNL results for the same fuel and source definitions.

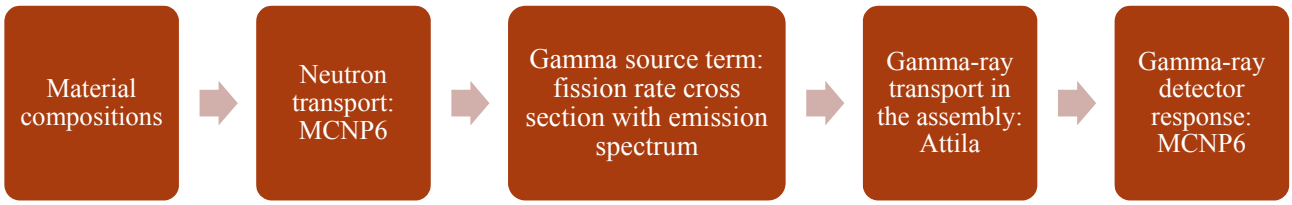

Figure 7. Schematic of PNNL's approach for modeling prompt fission gamma-ray signatures collected by HGET.

Next, the fission rates were used to calculate the prompt-fission-gamma-emission rate, using a ^{239}Pu prompt fission gamma spectrum [10]. Note that the ^{239}Pu gamma spectrum was used to approximate the spectrum for all fissile and fissionable isotopes for this initial scoping study. The published shape of that spectrum is shown in Figure 8, along with two different energy bin structures: 50-keV wide bins and a 24-group structure spanning from 0.05 MeV to 5 MeV. The 24-group structure is used as the input source term for the deterministic gamma-ray transport.

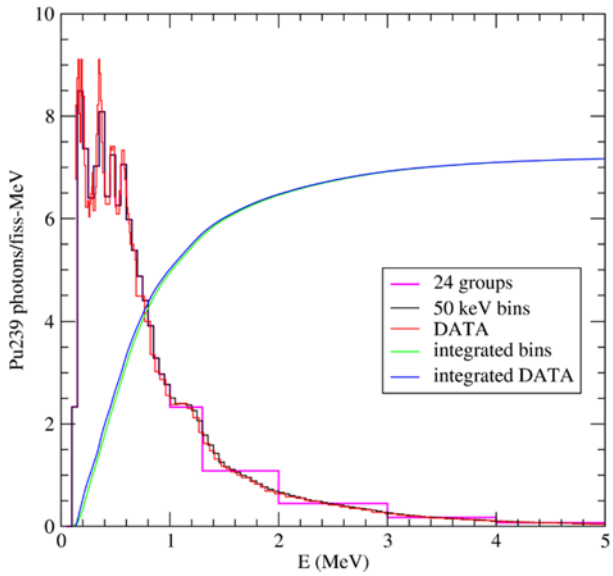

Figure 8. Prompt fission spectrum (from [10]) (red) with assumed group structure (magenta) for simulated pin photon sources based on pin fission rates. Integrated curves (green and blue) show total fission photons are preserved by group structure.

Transport of the photons out of the assembly and into the detector was performed using PNNL's Radiation Detection Scenario Analysis Toolbox (RADSAT), which is based on deterministic transport by the discrete-ordinates package Attila [20]. The emission spectrum from Figure 8 is propagated using 24 energy groups, with angular quadrature S_{16} P_2, and a mesh size of 2 mm in the pins. The angular flux is tallied at each detector location, using a last-collided flux tally with a custom angular quadrature (the collection of discrete angles used for calculation) to fully sample the angles incident on the collimator face. The angular flux is then sampled according to the opening angle of the collimator; the quadrature accounted for the umbra-penumbra effect but not for septal penetration through the collimator. This angular flux was then ported to MCNP to calculate a stochastic detector response. The full assembly detector response is calculated for 159 detector offsets (2 mm spacing) for 128 angles. Detector response is also calculated separately for each pin. This allows for the construction of assemblies with variations in composition, and it also fully characterizes system response to individual pins for use in inverse problems (tomography reconstruction). The RADSAT methods used for gamma-ray transport and detector response calculation in HGET are very similar to those employed by PNNL in the UGET Phase I Study; more complete descriptions of these methods can be found in [3, 21]. To build confidence in the accuracy of the deterministic gamma-ray transport, calculations were performed at multiple energy group structures, angular quadratures, spatial mesh sizes, and angular quadratures for the detector response to ensure that a stable and well-converged solution was achieved. Finally, hand-calculated estimates of detector response were made for outer pins showing order of magnitude agreement with numerical results.

4.3 Validation of Neutron Transport Calculations

As described in the two previous sections, PNNL (for prompt gamma rays) and LLNL (for delayed gamma rays) used very similar methods (i.e., MCNP6) for neutron transport and calculation of the induced fission rate. Absent empirical data on which to benchmark the HGET simulations, PNNL and LLNL used a comparative evaluation to provide confidence in the accuracy and consistency of the neutron-transport

calculations. For these comparisons, the neutron transport calculation results obtained by PNNL and LLNL in the HGETv1a instrument geometry were calculated. An example is shown in Figure 9, illustrating a comparison of the total D-T source induced fission rate distribution from PNNL and LLNL modeling. The two results demonstrate relatively good agreement in the relative induced fission rate, on a pin-by-pin basis. There are small discrepancies in isolated regions such as assembly periphery and corners—these discrepancies are attributed to minor differences in the details of the HGETv1a model, but are not considered significant in light of the fact that the HGET study is focused on proof-of-principle viability analyses.

The comparisons in Figure 9 provide confidence in the consistency of PNNL and LLNL neutron-transport calculations, as measured in the relative sense on a pin-by-pin basis. It is also important to demonstrate that the absolute magnitude of the induced fission rates are similar. For the MOXA assembly, PNNL's predictions for total fission rate in a 28-cm length of the assembly were: 4.41×10^7 for D-T and 4.41×10^5 for D-D. In comparison, the predictions for total fission rate from LLNL were 4.9×10^7 for D-T and 4.9×10^5 for D-D. These independent calculations for induced fission rate agree within approximately 11%, as depicted in Figure 10.

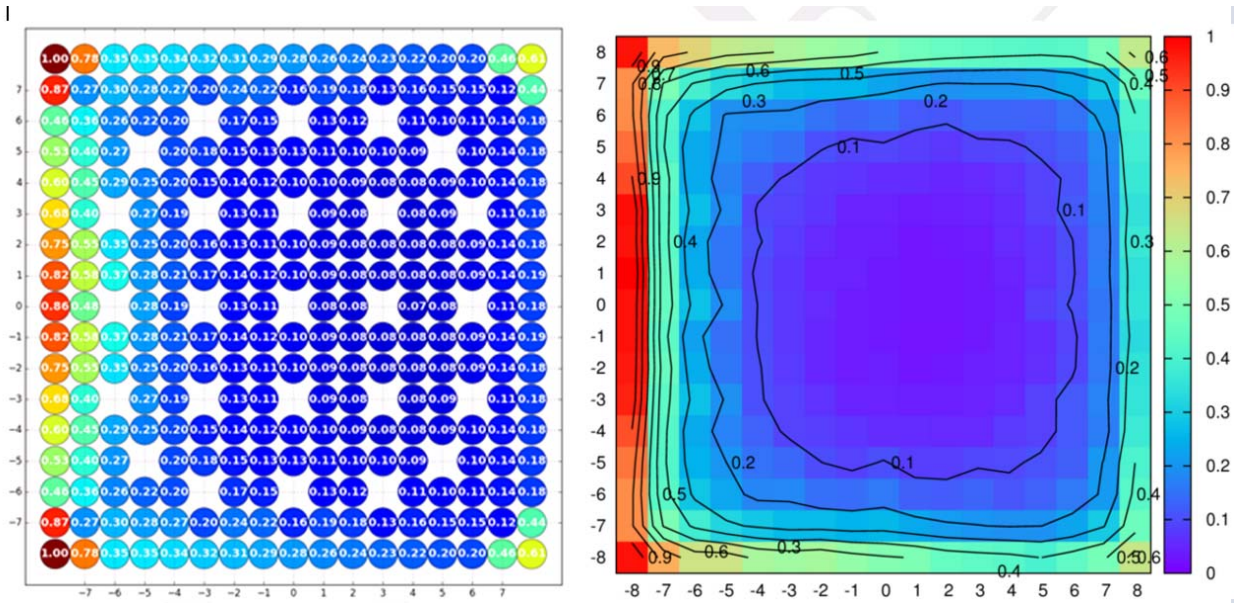

Figure 9. A qualitative comparison of the calculated induced thermal fission rate inside the 17x17 PWR MOXA assembly in the HGETv1a setup with a D-T source. LLNL-calculated result (left) and PNNL result (right).

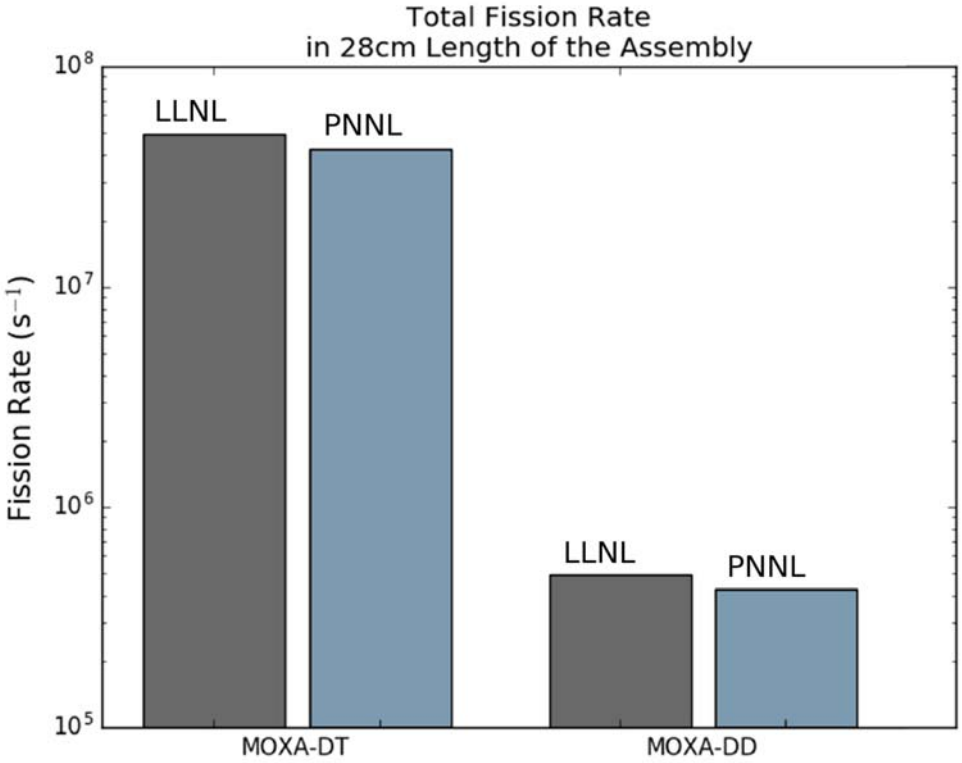

Figure 10. Quantitative comparison of induced fission rates in the MOXA assembly, as calculated by LLNL (for evaluation of delayed-gamma signatures) and PNNL (for evaluation of prompt fission gamma signatures) using independent MCNP simulations.

5.0 HGET v1 Design Study

Here we review the parameters and assumptions that went into the initial study, the design of the neutron reflector system to illuminate the assembly, and the design of the detector and collimator system to perform the imaging. As noted in Section 3, the production of high energy gammas is much lower in fresh fuel than in spent fuel, where gamma emission tomography has been successfully demonstrated. Even the highest flux signal investigated, the integrated prompt gamma emission, is still approximately 4 orders of magnitude lower than the spent fuel examined under the UGET SP-1 investigation. Thus, the neutron reflector/moderator must be designed to produce as much neutron flux as possible, and the gamma-ray detector and collimator are designed for higher efficiency and lower spatial resolution than for a spent fuel instrument.

As discussed in Section 2, it is assumed that measurement time should be on the order of an hour to be operationally relevant. Also, a maximum neutron moderator/reflector weight of 100 kg was enforced during the design study, on the logic that this represented a reasonable size for a mobile instrument deployed at a fuel fabrication or reactor facility. The calculations and preliminary performance predictions described in this report are based on the MOXA fuel assembly definition described in Section 2.

The neutron generator was modeled on an existing commercially available design, the Thermo Scientific P 385, which produces 3×10^{8} n/s at 14.1 MeV from the D-T reaction in a portable package (mass approximately 18 kg, will fit in a suitcase), or $3\text{x}10^{6}$ n/s at 2.5 MeV from the D-D reaction. Higher-intensity neutron generators may be available. For example, Phoenix Nuclear Labs offer a D-D neutron generator with a total mass of 250 kg, a meter-scale generator length and footprint for supporting equipment, and a neutron production rate of up to 5×10^{10} n/s. The output when the deuterated target is replaced by a tritiated target is stated to be 100 times higher (thus, up to 5×10^{12} n/s). While not exactly portable, it indicates that higher output instruments are available if necessary. Another example is the Starfire Industries nGen-310, a system with a mass of 6.3 kg that produces 1×10^{7} n/s using the D-D reaction. If modified with a tritiated target, an output of 1×10^{9} n/s would be expected. This illustrates that the D-T source assumptions made in this study are consistent with the desire for a cost-effective, highly portable device but that higher intensities are also possible, especially if concessions on size (e.g., for a fixed, rather than portable HGET device) are possible .

5.1 Moderator/Reflector Design Variants

A wide range of source/moderator/reflector designs and materials (e.g., poly, graphite, hydrided DU) were considered in the early stages of the HGET v1 design study. Both a D-D and a D-T neutron generator were considered; the lower energy neutrons from D-D produce a smaller background of ^{238}U fissions, at the expense of lower flux. The metrics for evaluating the various designs were: 1) uniformity of thermal and epithermal flux across the assembly cross-section, 2) total fission rate induced in the MOXA fuel definition, and 3) relative contributions of fissile and ^{238}U fission. Several of the early designs were discarded based on these metrics; Figure 11 depicts the two candidate designs that demonstrated the most promise: HGETv1a and HGETv1b.

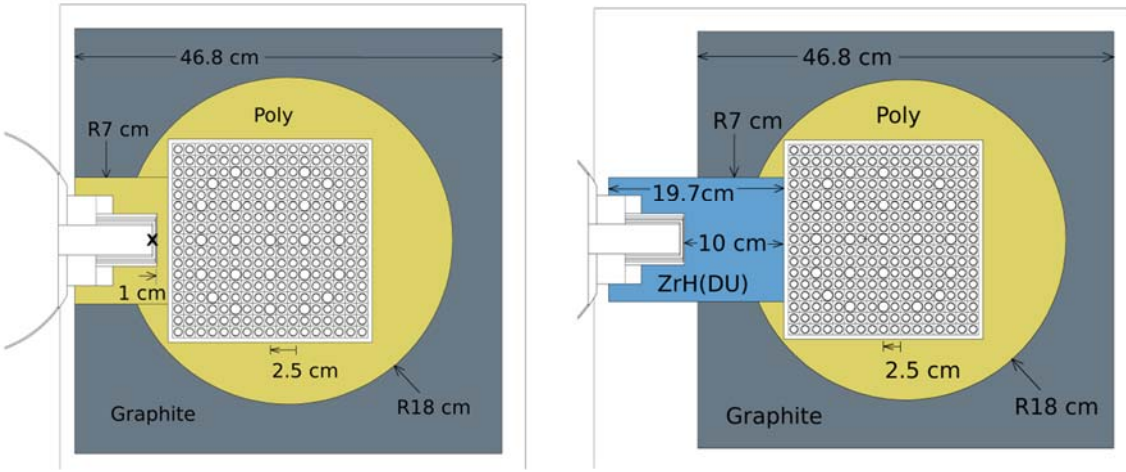

Figure 11. Geometry of two source/moderator/reflector designs for total flux and thermal flux fraction for assay of a 17x17 PWR assembly: HGETv1a (left) and HGETv1b (right).

Figure 12 shows the low-energy fission rate distributions for the HGETv1a and HGETv1b designs. Immediately evident is a relatively high fission rate on the source side of the assembly, in the outer row of pins. The neutron self-shielding effect, which depresses the fission rate on the interior of the assembly due to interactions between the neutrons and the fuel pins, is also clear. The overall effect is a gradient of approximately 10X between the fission rates at the outermost to innermost pins – although if the outer row of pins is neglected, the fission rate in the rest of the assembly is within a factor of ~3X and has a predictable gradient structure, with no highly localized changes on the interior of the assembly.

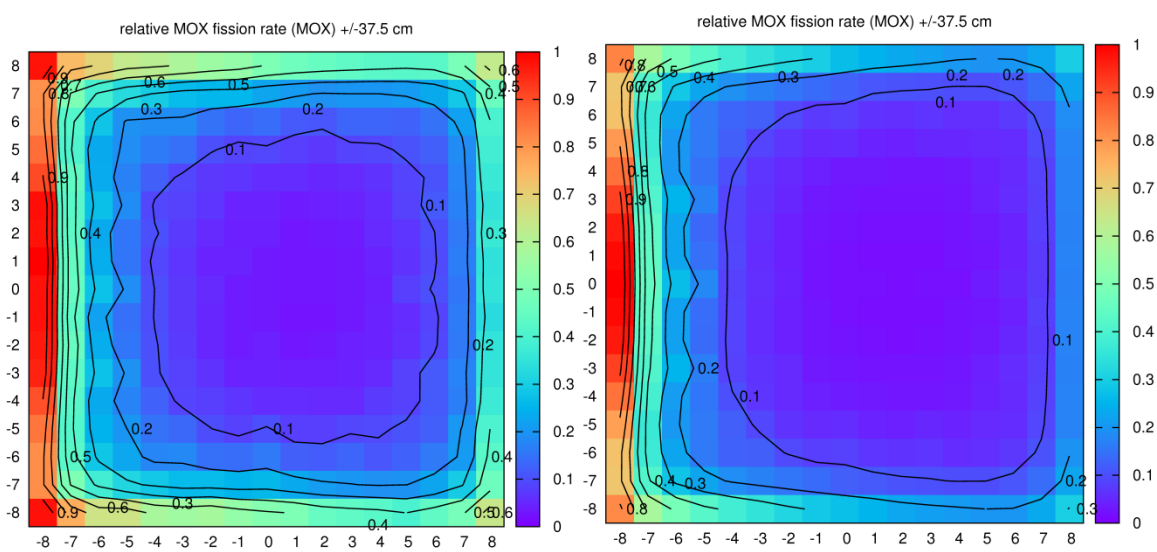

Figure 12. Relative thermal fission rate for HGETv1a (left) and HGETv1b (right). Each square represents one of the pins in the MOXA assembly definition.

Another factor important to the efficiency of the simulation studies is how much of the fuel assembly axial dimension must be included in order to adequately capture the axial variation in induced fission rate. The axial neutron flux profile in Figure 13 shows that, assuming the HGETv1 designs, a 28-cm segment of the assembly was sufficient to include over 90% of the induced fissions. An active length of 28 cm was assumed in the MCNP simulations of neutron flux, fission rate, and neutron-induced gamma-ray source terms.

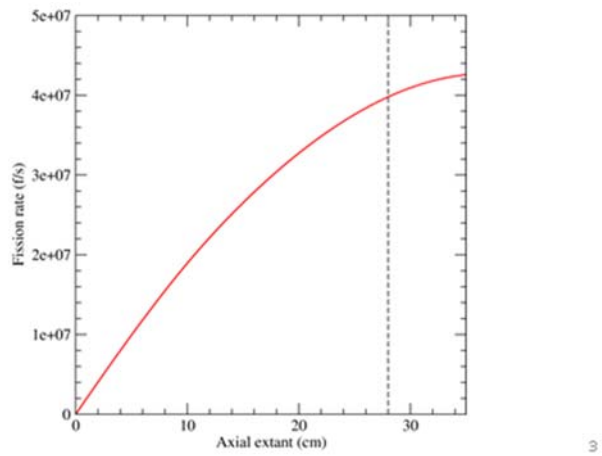

Figure 13. Total cumulative fission rate with axial assembly distance.

Figure 14 summarizes the physics trade-offs in attaining both high total fission rate and a high ratio of low- (primarily fissile isotopes) to high- (primarily ^{238}U) energy fission rates for various designs for the moderating plug placed between the source and the assembly.

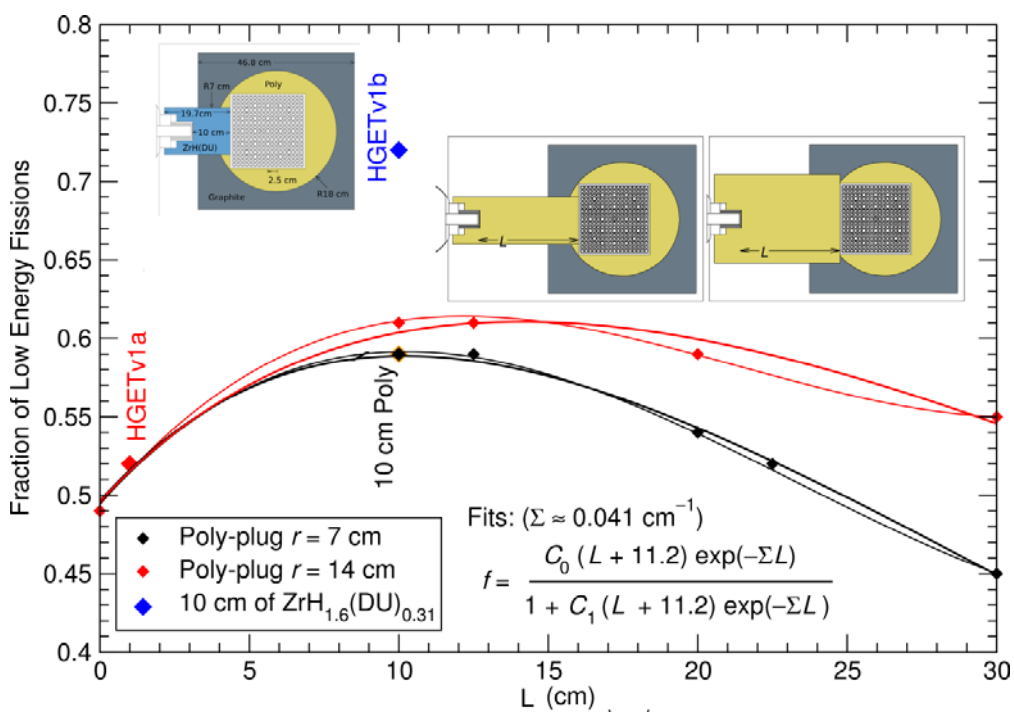

Figure 14. Comparison of fissions due to low-energy neutrons, for HGETv1a and HGETv1b designs, assuming different source-plug designs. The radius of the plug (r) and length of the plug (L) are varied for the two designs.

Clear from Figure 14 is that a greater moderator plug length (L) increases the low/high ratio until neutron capture begins to deplete the thermalized neutron flux, at about L=15 cm. Interestingly, the hydrided DU of HGETv1b provided a higher proportion of low-energy fissions and a higher total fission rate (Figure 15) than the case with the same length (10 cm) of poly due to (n,2n) reactions on ^{238}U.

Figure 15 provides a comparison of the total fission rates for various source/moderator/reflector combinations, and the relative contributions from various fissile and fissionable isotopes. Results for both the LEU and MOXA assembly are given.

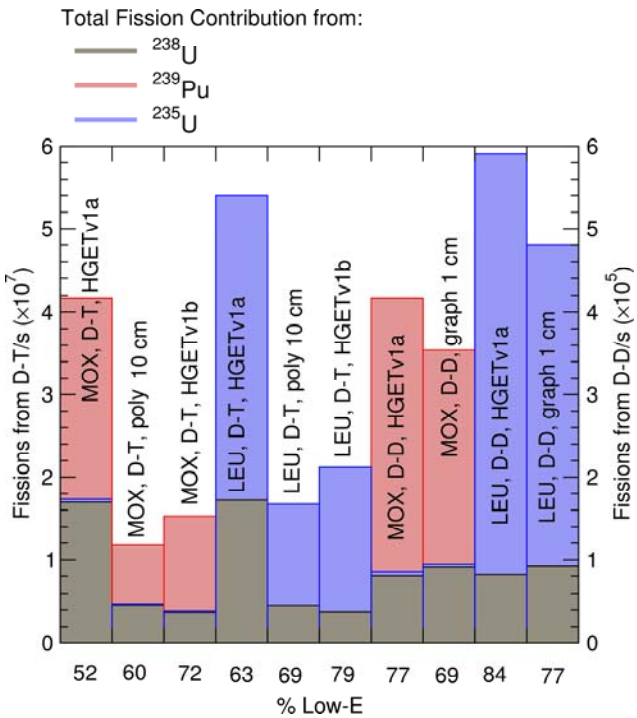

Figure 15. Performance of including HGETv1a and HGETv1b for MOX and LEU fuels, for various plug variants. Results are shown for both a typical D-T (3×10^8 n/s) and D-D (3×10^6 n/s) neutron generator source.

The first important observation from in Figure 15 is the very different total fission rates for the D-T and D-D. Cross-section limitations generally dictate that D-T source output will be approximately two orders of magnitude higher than the D-D output in the same form-factor. In the HGET studies, the interrogating neutron source strength was assumed at $3x10^6$ n/s for the D-D source and $x10^8$ n/s for the D-T source, which is consistent with the industry standards for portable neutron generators.

The second important message from Figure 15 is the relative portion of fission from the fissile isotopes as compared to ^{238}U. Since ^{238}U is the dominant isotope in the fuel matrix but is not the target isotope to be measured and verified by the IAEA, its contribution to the induced gamma-ray source term needs to be suppressed as much as possible. Because of the substantial difference in the source neutron energy, the D-D and D-T interrogation sources perform quite differently in terms of enhancing the fissile fission rate while suppressing the fast fission rate. The 2.45 MeV D-D source is more easily moderated and therefore, it is more conducive to probing fissile isotopes such as ^{235}U, Pu^{239}, and Pu^{241}. The 14.1 MeV D-T source,

assuming the same moderation as used for the D-D source, will produce a higher proportion of threshold reactions with the most notable and problematic being ^{238}U fission (threshold ~1 MeV). I

Figure 15 demonstrates that although the D-D source provides a more favorable isotopic distribution of the fission rate, its total rate is significantly lower than in the case of the D-T source. Because the HGET instrument is likely to be "signal-starved", the HGET team decided that initial performance analyses would be based on the higher-intensity D-T source, and that the challenge of improved isotopic discrimination would be left for future work. While HGETv1b has attractive attributes in terms of relative fissile fraction and total fission rate, it relative complexity in terms of design (including presence of depleted uranium) led to it being discarded as a pragmatic design choice for IAEA use. Therefore, HGET v1a with a D-T source is the nominal instrument design used in all of the performance discussions provided in this report.

5.2 Collimator/detector study

While the number of potential collimator/detector combinations to consider for a tomography system is nearly limitless, the HGET team decided to begin its design study at the IAEA's Passive Gamma Emission Tomographer (PGET), as described more fully in [3] and depicted in Figure 16 below. Though PGET is intended for verification of spent fuel, it seemed logical that a variant on PGET tailored for unirradiated fuels would benefit from a high degree of familiarity among tomography practitioners and the potential for leveraging of hardware components (e.g., detector arrays, pulse-processing electronics).

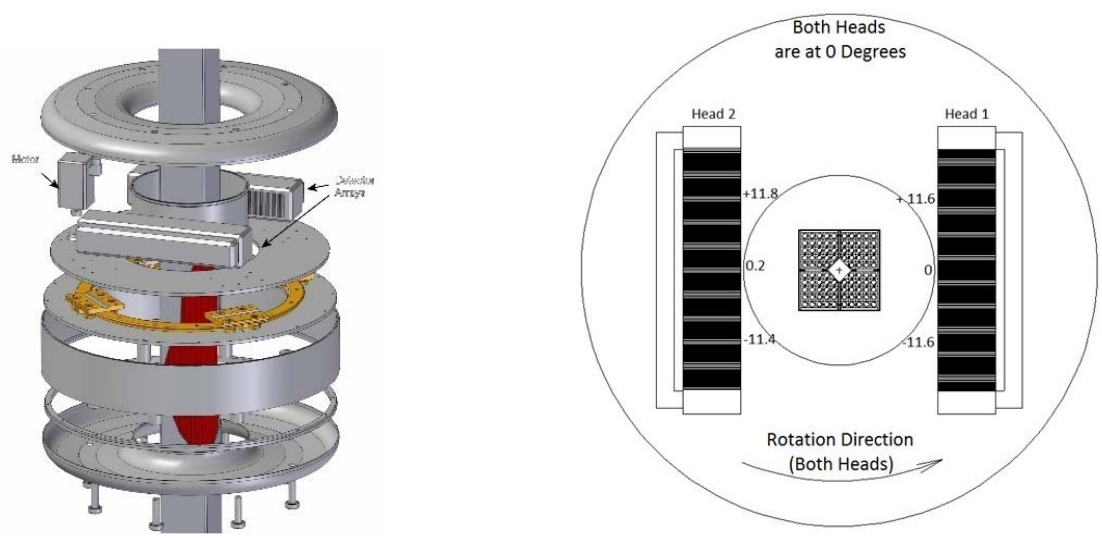

Figure 16. Rendering of the PGET instrument design including the housing and fuel assembly in the interrogation chamber (left), and vertical view of the detector heads containing 104 CdTe detectors in each head (right) [3].

As noted earlier, the central challenge in defining the HGET collimator/detector combination is to increase the collection efficiency significantly while preserving sufficient spatial resolution. The PGET collimator has an angled opening, 10 cm long, open 7 cm high at the front and 0.5 cm high at the back, and 0.15 cm wide. To increase the collection efficiency for HGET gamma-ray signatures, a collimator was proposed with a shorter length (5 cm), a parallel opening 7 cm high at both front and back, and 0.15 cm wide. This

increases the area on the detector from 0.075 cm^2 to 1.05 cm^2 compared with the PGET collimator (Figure 17). The change in angular acceptance of the detector results in a factor of 14 increase in count rate, with another 2x increase due to the larger detector area illuminated. The collimator opening along the pins can be opened to increase flux, but given the neutron profile along the pins described in Figure 13, the current design is a good match for the low-gradient portion of the neutron field. To take advantage of the decrease in collimator length, and further improve the overall collection efficiency, the front face of the collimator was moved 5 cm closer to the center of the HGET ring. This shift from 27 cm to 22 cm (as measured from the center of the ring) also helps to offset the loss of spatial resolution as the collimator length is decreased. The effects on spatial resolution are shown in Figure 18. The sinogram at left, from the PGET instrument, shows the clearest features; the HGET detector with the detector at 27 cm distance is the blurriest, at far right. The 22 cm distance provides spatial resolution intermediate to these cases, and is sufficient for high quality tomography reconstructions.

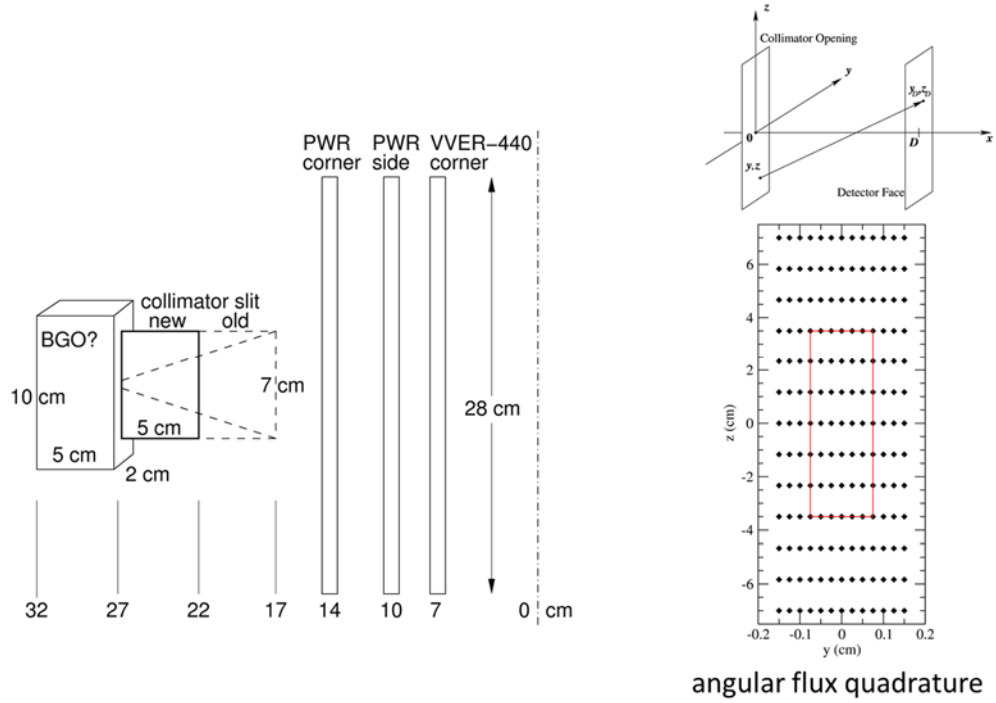

Figure 17. Left: Variants (bottom left) on HGET collimator designs (new) compared with existing PGET (old). Bottom right: quadrature angles defined on Cartesian grid for HGET collimator (bottom right). Resolution and intensity performance is highest for detector face at 22 cm.

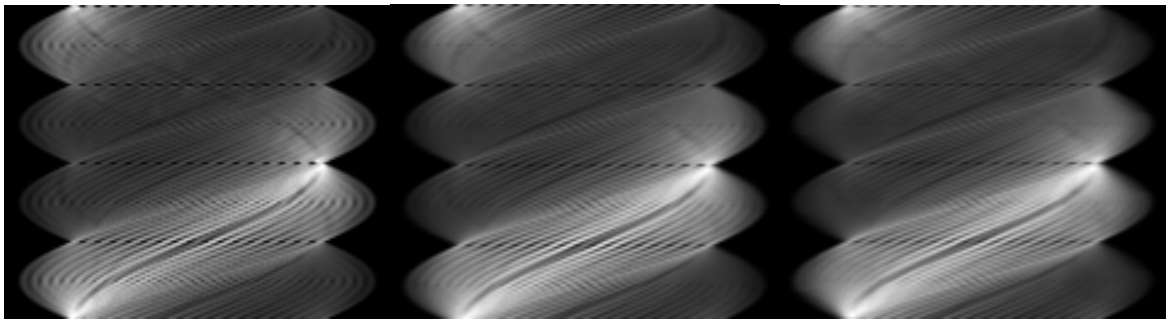

PGET **HGET@22cm** **HGET@27cm**

Figure 18. Qualitative comparison of collimator effects on spatial resolution using the sinograms from PGET and HGET variants with two different radial distances (22cm and 27 cm).

$Bi_4Ge_3O_{12}$ (BGO) was chosen as the nominal gamma-ray spectrometer material for the HGET v1a design for several reasons. First, its high density and atomic number translate to high stopping power for higher-energy gamma rays, whilst maintaining a relatively small form factor that can support a highly arrayed detector arrangement like the one used in PGET. Importantly, BGO is a very common material for positron emission tomography systems used in nuclear medicine, which means that large arrays of relatively small voxels are readily available in the commercial market. BGO has significantly poorer energy resolution than other candidates such as NaI(Tl), CZT or $LaBr_3$, but energy resolution is not expected to be a dominant performance effect, assuming that HGET data collection relies on broad energy windows for collection of prompt-fission or delayed fission gamma rays.

The nominal size of the BGO crystals in the HGET v1 design was defined largely by the available space behind the collimator openings, and the actual size of the aperture in the collimator. A 7-cm crystal height was chosen to match the back opening of the collimator and the neutron-illuminated region of the assembly (
Figure **17**); little performance improvement was gained by increasing this to 10 cm. Figure 17 also indicates a 2 cm width BGO crystal, which was used for initial calculations. Ultimately, a width of 0.3 cm was chosen to allow a collimator slit separation of 0.4 cm, as in the PGET design. Such a collimator arrangement ensures that the HGET instrument needs only rotational, not translational, movement of the detector heads, thereby providing reduced size and complexity in the instrument design. The simulation results in Figure 19 provide example pulse-height spectra for BGO crystals responding to a prompt-fission-gamma flux. This figure also provides support for the choice of a crystal depth of 3 cm: the penalty in collection efficiency in going from 5 cm to 3 cm in depth is relatively low, compared to the potential cost savings in detector and shielding material. Based on the modeling and analysis above, all performance estimates in this FY16 report are based BGO crystals that are 0.3x7x3cm.

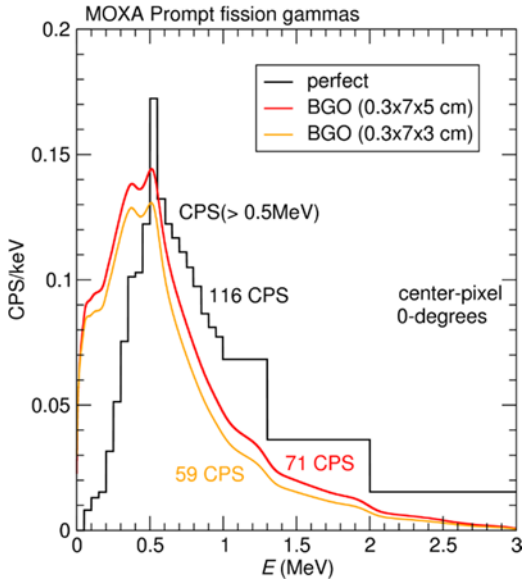

Figure 19. Detector response for prompt fission gammas for two BGO crystals behind a center-collimator slit. Integrated counts per second (CPS) are for E > 0.5 MeV.

The BGO detector is observed to give a factor of 3x improvement in efficiency compared to the original PGET detectors. This, combined with the 28x enhancement to count rates due to changes in the collimator geometry, results in approximately two orders of magnitude more counts at the detector relative to the PGET design, thereby helping to recover a significant portion of the signal discrepancy (several orders of magnitude) between the spent fuel applications for which PGET was originally designed and the HGET scenarios for unirradiated fuels.

6.0 Reconstruction Algorithms

For tomography, emission intensity data is collected as a function of position across the object and projection angles through the object. This data is commonly displayed in the form of a sinogram, as seen in Figure 18. A point feature in the object makes a sinusoidal track as a function of angle, with the amplitude indicating radial distance from the center of rotation and the phase indicating the angular position of the object. In the sinogram, multiple features overlap and add differently at each angle; the reconstruction problem is to map this intensity back to real space. The problem is further complicated by issues of finite spatial resolution, which changes across the field of view due to the finite opening angles of the collimators, the presence of both primary and scattered radiation, and the fact that objects not only emit radiation but also absorb it. Background effects are also present, either due to scattered radiation which is distributed across the assembly, or due to source terms other than prompt fission gammas.

Algorithms for emission tomography of spent fuel have been investigated and applied under the UGET project, which focused on passive emission from spent fuel, and are described in [3]. In the discussions below, candidate reconstruction algorithms are described in the context of the unique features of the HGET verification scenario, most notably the relatively weak signatures and particularly extreme attenuation gradients.

6.1 Filtered Backprojection

The simplest approach to tomographic reconstruction is filtered backprojection, which solves analytically for the distribution of emissions, assuming that measurements are spaced at equal angles and that attenuation is minimal. This approach has the advantage of being both fast and requiring few assumptions about the system [22], and has been successfully used to locate missing pins in spent nuclear fuel [3]. However, since FBP in its simplest form makes no assumptions about attenuation, it cannot correct for the highly attenuating pins that block emissions from the center of the assembly. This leads to a reconstructed image which is systematically lower in intensity inside the assembly.

The case of fresh fuel is different from the spent fuel application in two important ways. First, the emission intensity is much lower, indicating that without other modifications a much longer measurement time will be needed. Second, emission intensity is a function not only of fuel composition, but also of illumination by the neutron field. Achieving a high and relatively uniform flux of thermal neutrons in the center of a large assembly is difficult, as seen in Section 5. The difference in counts at the detector from inner pins to outer pins is already large in passive emission tomography, but neutron interrogation adds another significant gradient, on the order of 10X, between inner and outer pins. Reconstructing a dataset with such an extreme gradient results in poor image quality, as seen in Figure 20, where the artifacts from the outer pins overwhelm the signal from the inner pins.

6.2 Model-based reconstruction

Although the simplest approach to tomographic reconstruction struggles with the low count rates and large intensity gradients, fresh (and spent) fuel verification by the IAEA is fundamentally a confirmatory measurement. This means we can use *a priori* information about a declared assembly to improve reconstruction. There are a number of ways to incorporate this information, but one straightforward

approach is to assume a declared assembly geometry and solve for average emission values for each pin. Mathematically, this is phrased as measurement data (g_α) with α as the sinogram angle/offset index according to

$$g_\alpha = \sum_k H_{\alpha k} f_k \tag{1}$$

where f_k is the reconstructed activity estimate, here with k as the pin index, and $H_{\alpha k}$ is the model based system response matrix, in this case the detector response to each possible emitting pin in the presence of attenuation due to the whole assembly. This approach is described more fully in the UGET final report [3]. This choice incorporates known information about the detector and the attenuation properties of the pin assembly, and greatly reduces the number of variables over a pixel-by-pixel approach.

To illustrate the effects of using a model-based reconstruction a set of synthetic measured data g_α is constructed, for a PWR LEU assembly with eleven missing pins, equal emissions from each pin, and Poisson noise; and measured using the original PGET instrument geometry. To simplify the analysis, relative to the full coupled neutron-gamma problem, we use passive gamma emissions at a relevant energy, in this case the 1001 keV line of ^{234m}Pa (from the ^{238}U decay chain). We adjust the integration time arbitrarily to achieve counting statistics relevant to the induced fission problem. Because the emission rate for LEU at 1001 keV is only 343 γ/cm/s, a 1 year integration time is used unless otherwise noted. Note that this is not intended as a suggested assay technique, but as a simplified means of exploring tomographic reconstruction techniques.In these problems, emissions are reconstructed on a pin-by-pin basis, rather than as individual pixels, so each score represents an average value over the pin. This integration time should not be taken as representative of the HGET approach or instrument, but provides a reference point for comparing between methods and Poisson noise levels.

In Figure 20, the reconstructed pin values are shown, in arbitrary units, as a function of distance from the assembly center. On the left, the reconstruction is done using a model-independent method (FBP); on the right, a model-based reconstruction is shown with a model well matched to the data.

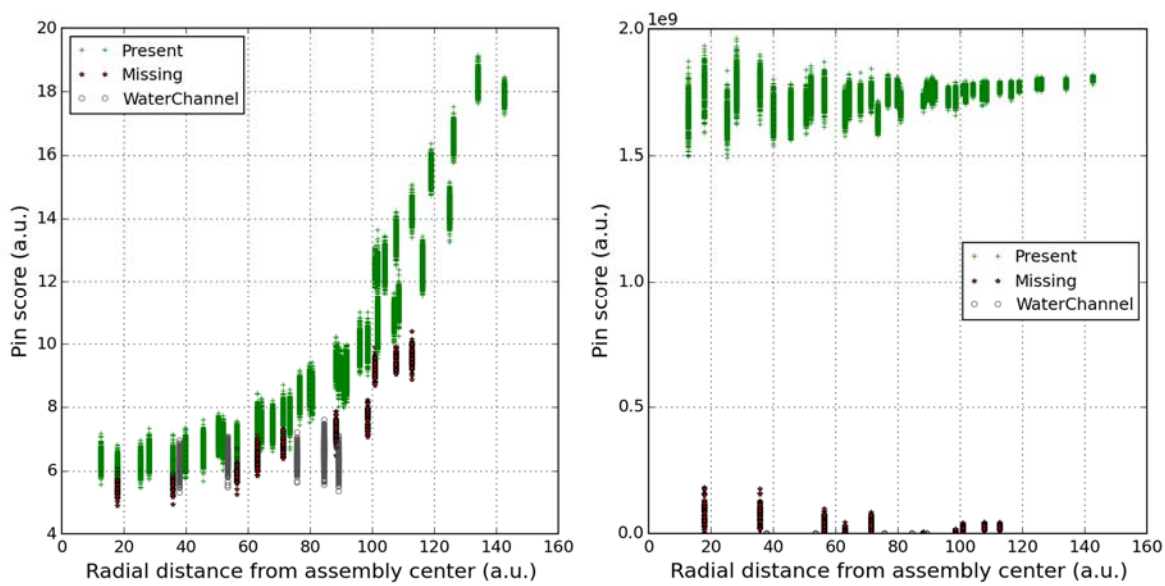

Figure 20. Reconstructed pin scores as a function of radial distance, using filtered backprojection (left), and a well-matched model-based reconstruction (right). Key assumptions: PGET instrument design, 1001 keV line for LEU, total assay time of 1 year.

The FBP reconstruction shows a factor of three variation in pin intensity between inner and outer pins, due to the high attenuation of inner pins by outer pins which is not accounted for in the reconstruction. Further, it is very difficult to distinguish missing pins, particularly towards the interior of the assembly. Using a model-based reconstruction, although pin scores vary more towards the interior due to counting statistics, the overall trend correctly predicts similar pin scores across the assembly. The missing pins are readily identifiable in this example used to illustrate the benefit of model-based reconstruction algorithms.

The difficulty with such a model-dependent approach lies in recognizing whether the right model is being used. If a pin is missing, this changes not only the emission map that we're trying to reconstruct, but also the attenuation map, which is built into the system matrix $H_{\alpha k}$. New reconstruction methods, specific to the HGET application, are required in order to solve this highly coupled emission and transmission problem. Below, a series of approaches is described which were developed in an attempt to meet this challenge. For testing purposes, these examples start with passive emissions of the 1001 keV line for a PWR assembly with 11 missing pins, but the observations can be generalized to other cases.

6.2.1 Bootstrap Method

One characteristic of fuel pin tomography is that pins on the outside of the assembly are much easier to reconstruct than pins on the interior, due to the large relative count rate differences in the signals collected from outer and inner pins. Here, this observation is used in order to sequentially improve the pin model in a bootstrap fashion that progresses from the exterior of the assembly to the interior. In the initial step, all pins are assumed present in the reconstruction. From this first set of pin activity scores, a few outliers can be identified as candidate missing pins based on an intensity that is significantly lower than its neighbors (and/or the declared nominal composition). These asserted missing pins are analytically removed from the model and reconstruction is performed again with the new model. The changes to the model due to missing pins is approximated by geometrically removing the attenuation effect of missing pins by including an α *and* k dependent factor

$$g_\alpha = \sum_k H_{\alpha k} \exp\left[\mu^{(0)} \sum_j l_{\alpha k}^{(j)} \left(1 - b_j\right)\right] f_k \tag{2}$$

where $H_{\alpha k}$ has no missing pins. The Eq. (2) internal sum (j) is over missing pins with $l_{\alpha k}^{(j)}$ as the length intersected on a line through pin j from pin k on the way to angle/offset α, $\mu^{(0)}$ is the attenuation coefficient of UO_2 and b_j is a scaled attenuation variable taken as one for pin "present" and zero for "pin absent".

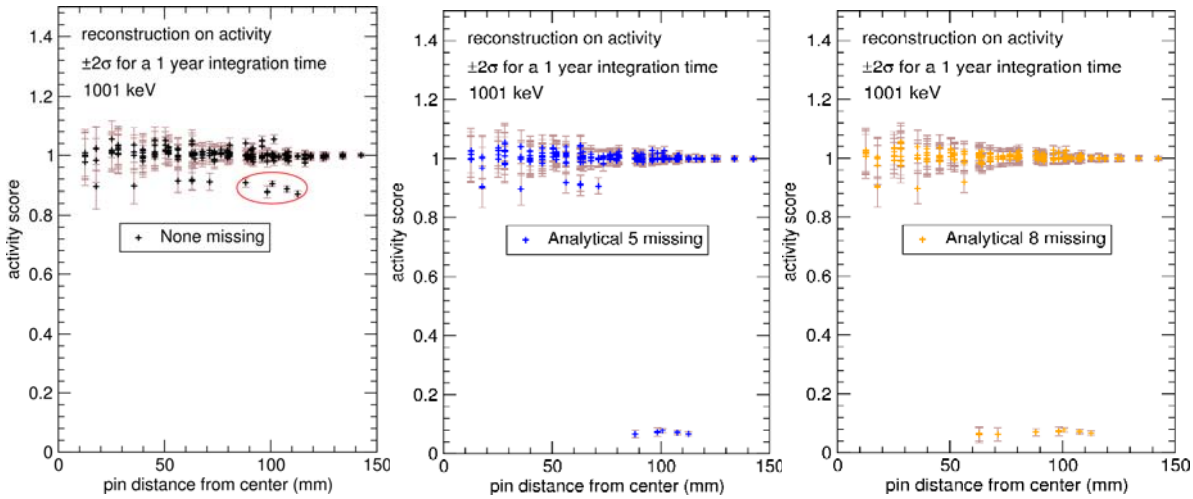

Figure 21. Illustration of bootstrap method for including potential missing pins in a model-based pin-activity reconstruction process: Step 1 where all pins assumed present (left); 5 of the 11 missing pins are significantly different and can be identified as missing. Step 2 where five pins assumed missing based on outliers in Step 1; Step 3 where three more pins are assumed missing (total of 8) based on outliers in Step 2.

Taking the Eq. (2) j sum over the 5 most separable missing pins of (Figure 21, left), we find that an additional missing pin becomes statistically separable (Figure 21, center). Including more known missing pins seems to add no value for this case (Figure 21, right) – although correcting the model improves the reconstruction quality in the immediate vicinity of the missing pin, the effect on the overall reconstruction quality is mostly local. Although this method may help identify some missing pins, it is insufficient on its own to address the combined attenuation and emission reconstruction.

6.2.2 Attenuation Map vs. Activity Map, and Joint Solutions

A second approach to selecting the most appropriate system response function is to explicitly solve for both pin activity and pin attenuation. This approach starts by considering two extreme assumptions. First, it is assumed that all variations in the reconstruction are due to activity variations, and the attenuation map is fixed. This is essentially the initial approach to the problem, reconstructing activity with known attenuation. However, it is also possible to interpret the measured data under the opposite premise, that all variations in the reconstruction are due to attenuation variations, and the emission map is fixed.

Figure 22 (left) shows the results of both reconstructions, where the horizontal axis is the reconstruction based on solving for f_k with all pins present [Eq. (2)] with flat attenuations all $b_j = 1$; and, the vertical axis is based on solving linearized Eq. (2) for b_j and mean activity $\langle f \rangle$ assuming flat activities $f_k = \langle f \rangle$.

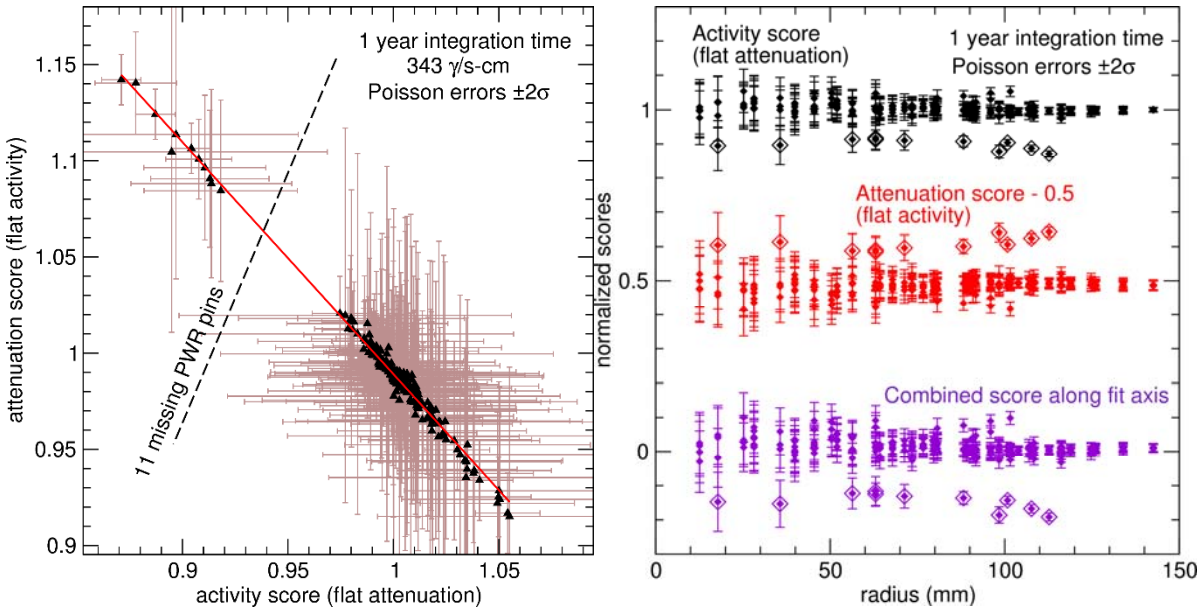

Figure 22. Independent reconstruction of activity with flat attenuation and attenuation with flat activity (left). The error reduction obtained (purple) for a combined score (right); missing pins are indicated by an outer diamond around the symbol.

The pin values for activity and attenuation fall along a line for both present and absent pins, with higher activity scores corresponding with lower attenuation scores. Note that the attenuation scores for the missing pins are greater than one instead of less than one. This is because the flat activity assumption for missing pins, having zero activity, artificially results in an increased "self" attenuation to account for the sinogram data. The right side of Figure 22 shows pin score as a function of distance from the center of the assembly for attenuation only, activity only, and relative to the linear fit from both reconstruction methods. While activity and attenuation scores give roughly the same statistical separation for missing pins, a combined metric orthogonal to the "fit-axis" (red line) of Figure 22 (right) allows all but one pin to be statistically separable based on two-sigma statistical error bars.

While this analysis is promising, an ideal solution would solve simultaneously for attenuation and activity – and would avoid the seemingly unphysical missing pin attenuation scores resulting from the flat activity assumption. A simultaneous reconstruction of both activity f_k and attenuation b_j can be achieved by solving Eq. (2) iteratively to convergence. An application of a similar method to Time-of-Flight PET is given in [23]. Figure 23 shows that convergence is quickly reached after 3-4 iterations where the initial scores (0th iteration) are assumed to be the independently obtained scores of Figure 22. It is physically reassuring that the attenuation scores become less than one, but because of the greater dimension (2X) of the system matrix and the iterative propagation of error, the error on the converged solution tends to grow with the greater separation obtained from the reconstruction. While the results are more physically reasonable, the ability to segment missing pins from present pins is not enhanced.

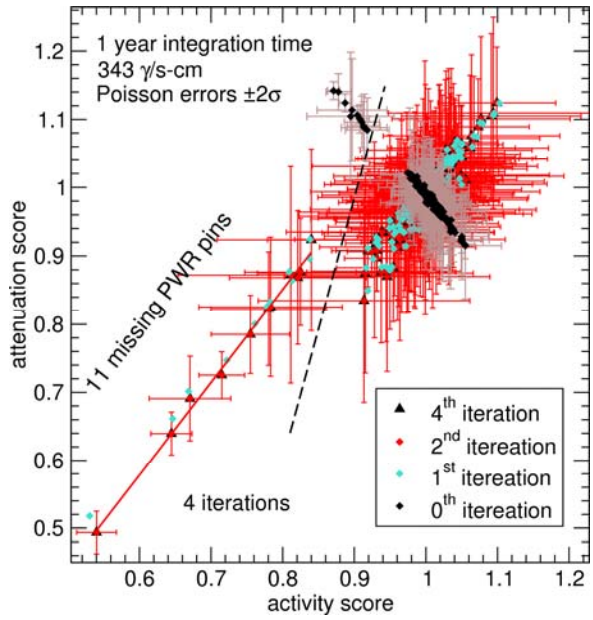

Figure 23. Simultaneous reconstruction of activity and attenuation. Results are shown prior to iteration (black circles), and after 1 (green), 2 (red, with error bars), and 4 (black triangles) iterations. Note that little change occurs after the first iteration.

Although joint solutions for attenuation and activity are in principle of high interest, we find only modest improvements to pin segregation using this method. A small effort in FY17 may be directed towards investigating additional possible constraints on this approach.

6.2.3 Multi-Configuration Analysis

Another possible approach is based on identifying a finite set of possible single pin responses, with different missing pin configurations, and observing which set of responses best explain the observed data. Mathematically, this is done by restricting to a finite set of possible transfer matrices $H^{(j)}$, and the reconstruction can once again be recast as a linear equation

$$g_\alpha = \sum_{j,k} H^{(j)}_{\alpha k} f^{(j)}_k$$

The index j could refer to, for example, the set of fuel pins which are missing from an assembly. Ideally, the physical system would have $f^{(j)} = 0$ for all j except for the j corresponding to the physical configuration. For a poorly determined system or one with significant noise, the reconstruction could return a superposition of configurations. For consistency of notation with usual linear algebra conventions, j and k can be combined into a single superindex $[jk]$ in the product space of j and k

$$g_\alpha = \sum_{[jk]} H_{\alpha[jk]} f_{[jk]}$$

Including every possible combination of missing pins is unwieldy, so for a first pass the configurations are restricted to all pins present, or a single missing pin. The subsequent analysis can then be repeated for each pin in the assembly to locate likely candidates for which pins are missing. This is a good approximation of the full range of responses when the signals from missing fuel pins are largely local, but even for less

localized behavior provides a useful first case. This reduces the computational load and limits confusing cases where a superposition of many configurations is returned.

6.2.3.1 Refinements

It is expected that the effect of a missing pin will be largely local - nearby pins may contribute different amounts to the sinogram signal g, but distant pins will have nearly the same contributions. This means that for two different configurations j and j' differing only by the presence or absence of a single pin, most columns of $H_{\alpha[jk]}$ will be indistinguishable from the corresponding columns of $H_{\alpha[j'k]}$. This results in a highly degenerate matrix. The pseudo-inverse can still be constructed, but the resulting reconstruction will be riddled with ambiguities. Worse, H is degenerate in uninteresting ways -- mixing up different configurations j of distant pins k doesn't tell us anything interesting about the presence or absence of the pin in question.

This leads to a suggested re-ordering of the second index ($[jk]$) of H. Whenever the columns of two different configurations differ by less than some threshold, drop one of the columns and delete the corresponding element of f.

In addition, it is known with certainty that the element of f corresponding to any missing pin is zero. In other words, that pin never contributes any signal to the sinogram. All the information in the problem can be preserved if that element is dropped and the corresponding column of H is deleted. This will help to prevent un-physical reconstructions that result in a missing pin with non-zero activity.

Denoting this new index as l, and defining the dimension m such that l ranges from $1 \cdots m$, it can be seen that any given l can be mapped to any pin k and may correspond to one configuration j or may include the effects of both configurations. Any given combination of $j$and k can be mapped to one and only one l unless that j and k correspond to a missing pin.

6.2.3.2 Reconstruction

Analysis of this problem begins by performing a singular value decomposition of the transfer matrix $H_{\alpha l}$

$$H = UWV^T$$

where U is column-orthogonal with dimensions of $\nu \times m$, V is orthogonal with dimensions $m \times m$, and W is diagonal with dimensions $m \times m$. The diagonal elements of W are called the singular values. If any singular values are zero or negligibly small, the corresponding columns of V will not contribute to the signal. In other words, those columns of V corresponding to vanishing singular values form the null-space of H. Because V is orthogonal, it forms an orthonormal basis space onto which f is projected -- columns of V thus correspond to patterns of pin activity significant for analysis.

If the dimension of the null-space is zero, detection of the missing pin is accomplished by finding the pseudo-inverse of $H_{\alpha l}$

$$\widetilde{H}^{-1} = VW^{-1}U^T$$

and computing

$$f_l = \sum_{\alpha} \widetilde{H}^{-1}_{l\alpha}\, g_\alpha$$

If f has high activities within the missing-pin-only subspace and low activities within the full-assembly-only subspace, then a missing pin has been found.

If the null-space has dimension of greater than zero, then the corresponding columns of V identify degrees of freedom on pin activities that have no effect on the measured sinogram. If these columns include mixtures of both configurations included in the analysis, then it will be impossible to analytically distinguish whether an assembly with an arbitrary set of pin activities has pins missing. Identification of missing pins will therefore hinge on initial assumptions about what the pin activity patterns are expected to look like.

6.2.3.3 Method Test

A 17×17 PWR assembly with 11 missing pins was simulated and a measurement sinogram produced. Transfer matrices were produced for an assembly with no missing pins, 11 assemblies where one of the missing pins was removed, and 11 assemblies with a pin removed than was not one of the actual missing pins from the simulated signal. Two-configuration transfer matrices were created for each of the 22 candidate missing pins consisting of the missing pin configuration and the no missing pin configuration.

If h_i is the i-th column of the one-configuration transfer matrix H, then columns from both configurations were included if

$$\frac{\left|h_i^{(j)} - h_i^{(0)}\right|^2}{\left|h_i^{(j)}\right|\left|h_i^{(0)}\right|} > 0.01.$$

Otherwise, the column of the two-configuration H was filled with the mean of $h_i^{(j)}$ and $h_i^{(0)}$.

The resulting reconstructed activities could not distinguish between pin-present and pin-absent configurations: the activity tended to be evenly distributed between configurations. Singular vectors associated with the additional configuration were identified by taking the difference between the reconstructed activity vectors of the two configurations and finding those with the largest norms. This reliably identified singular vectors whose activity varied primarily among the set of pins that included both configurations. The singular vectors introduced by the incorporation of both configurations of a pin (each pin that could be in either configuration expanded the dimension of the H matrix by one and introduced a new singular vector) had singular values that clustered among the smallest of the singular values produced, and the smallest singular value was invariably from this set of singular vectors. While not mathematically exactly singular, the matrices were ill-conditioned, with condition numbers on the order of several hundred. The condition number of $H^{(0)}$ was 17.1, indicating that considering the presence or absence of a pin resulted in a much less well conditioned matrix.

6.2.4 Pattern Matching for Missing Pins

When augmenting H with a missing pin configuration results in a system that is ill-conditioned or singular, it is not always clear which linear combination of singular vectors gives the expected pattern found by reconstructing an assembly with a missing pin when assuming all pins are present. To overcome that difficulty, the patterns resulting from a mismatched model assumption can be checked for directly. This starts with an assumed vector of pin activities, $f^{(0)}$. This may be uniform if measuring passive emissions from U-238, or the simulated fission rates under active interrogation in the case of reconstructing on fission gamma rays. Let $H^{(0)}$ be the transfer matrix with all pins present.

Then

$$g^{(0)} = H^{(0)} f^{(0)}$$

is the sinogram which would be measured from the assumed pin activities. The reconstructed "perfect" activity is then

$$\tilde{f}^{(0)} = \left[\tilde{H}^{(0)}\right]^{-1} g^{(0)}.$$

Now assume that a pin j is missing. Its activity in the f-vector is set to zero. If necessary, the other pin activities can be adjusted (for example, to account for neutron shadowing effects during active interrogation). This gives an activity vector $f^{(j)}$. Find the resulting sinogram

$$g^{(j)} = H^{(j)} f^{(j)}$$

and then reconstruct the activity assuming all pins are present

$$\tilde{f}^{(j)} = \left[\tilde{H}^{(0)}\right]^{-1} g^{(j)}.$$

The difference between $\tilde{f}^{(0)}$ and $\tilde{f}^{(j)}$ represents the pattern of activity around pin j that we expect if pin j is missing. For computational purposes, however, what is useful is to subtract off the projection of $\tilde{f}^{(0)}$ on $\tilde{f}^{(j)}$ from $\tilde{f}^{(j)}$. This is done using the Gram-Schmidt method

$$\delta f^{(j)} = \tilde{f}^{(j)} - \frac{\tilde{f}^{(j)} \cdot \tilde{f}^{(0)}}{\tilde{f}^{(0)} \cdot \tilde{f}^{(0)}} \tilde{f}^{(0)}$$

To look for the pattern of activity indicative of a missing pin, a measured activity vector is reconstructed from the measured sinogram g_m assuming all pins are present

$$f_m = \left[\tilde{H}^{(0)}\right]^{-1} g_m$$

Then the measured activity vector is compared with predicted missing pin patterns by taking $f_m \cdot \delta f^{(j)}$. If all pins are present, or pins are missing which are far from j, f_m should be close to $\tilde{f}^{(0)}$ and the product should nearly vanish. If pin j is missing, then the dot product should return a much larger number.

An alternate method would be to use patterns within the measured sinograms directly. This would be done by calculating

$$\delta g^{(j)} = g^{(j)} - \frac{g^{(j)} \cdot g^{(0)}}{g^{(0)} \cdot g^{(0)}} g^{(0)}$$

and finding the projection $\delta g^{(j)} \cdot g_m$. At this point, it is not clear if this method would be better, worse, or identical to looking for patterns of activity among the pins.

This method has not yet been tested. Performing this analysis and testing for sensitivity to missing pins is planned for next FY.

7.0 Preliminary Performance Predictions

Previous sections of this report describe the candidate HGET signatures, modeling methods, nominal HGETv1a design, and initial development of HGET-specific reconstruction methods. In an effort to shed initial light on the potential performance of an HGET instrument, all of these elements were connected as a vehicle for preliminary predictions of HGET performance.

In this first round of performance prediction, only the prompt-fission gamma-ray signal has been considered, and a straightforward model-based reconstruction on a pin-by-pin basis (i.e., no bootstrap or other candidate advanced technique) was used to bound the tomography inversion problem. The primary question to be addressed was: Based on the HGET v1a design, the MOXA assembly definition, anticipated operator declarations, and simulated prompt-gamma signatures, can reasonable uncertainties be achieved for fissile-mass concentration on a pin-by-pin basis within 1-2 hours? The achievable uncertainties for HGET verification of fissile-mass concentration at the *pin level* are then compared to the ITVs for fissile-mass determination *at the assembly level* using PNCL.

The end-to-end HGET analysis process is shown in Figure 24 and described here. The starting point is the forward calculation of pin-by-pin fission rates, by isotope, using MCNP. This step is shown at the upper left in Figure 24 and is based on the assembly under consideration (here, the PWR MOXA definition with 11 missing pins) and the HGETv1a design. Using pin-by-pin, isotope-specific fission rate calculated using MCNP, the pin-by-pin prompt fission gamma source term is calculated. That gamma-ray flux is then transported from the pins to the front face of the detectors (upper middle in Figure 24) using RADSAT, and culminates with the calculation of detector response, including Poisson noise commensurate with the measurement time. These data form the detector-response sinogram g_α, in terms of absolute count rates (cps for a specific detector at a specific angular orientation), and therefore the simulated response of HGETv1a to the MOXA assembly. In actual implementation, of course, the g_α data would be measured.

With the forward calculation of HGET response in hand, the inversion and analysis steps begin. As discussed previously, RADSAT was used to calculate a pin-based system response function $H_{\alpha k}$, where k is the pin index and α the sinogram index. In this initial performance study, the system response function assumed that the operator has declared (accurately) that 11 specific pins are missing, and that information is included in the inversion process via the system response matrix. Using this model-based system response matrix, the synthetic data can be inverted using a least squares solution [3] to recover the pin-by-pin fission rates in the assembly. It is important to note that in this initial performance study, RADSAT was used for both the forward transport of the prompt fission gamma-ray signal and the calculation of the system response for inversion. This is a best-case scenario that is convenient and useful for predicting the upper bound of HGET performance and associated statistical uncertainties, but as previous GET studies have shown [3], using the same transport method for both forward and inversion steps will underestimate the systematic errors that arise when the forward (or measured) data is generated independent of the method used to calculate system response.

Next, the pin-by-pin fission rate produced by the tomographic inverse problem must be translated to the verification parameter of interest: fissile-material concentration. De-tangling the fissile concentration from the fission rate must recognize that fission from non-fissile isotopes, most notably ^{238}U, can contribute significantly to the total induced fission rate, but the concentration of the non-fissile isotopes is not the IAEA verification parameter of interest. Such a translation can be complex since the fission cross-sections

for the fissile and fissionable isotopes are highly dependent on incident neutron energy (including resonance structures and threshold reactions), and the neutron energy spectrum varies by pin location—due to attenuation from surrounding pins and attenuation within the pin of interest due to its own fissile loading. Reporting the pin-level Fissile Pu fraction is the outcome of the modeling and analysis framework, as depicted in the lower right of Figure 23.

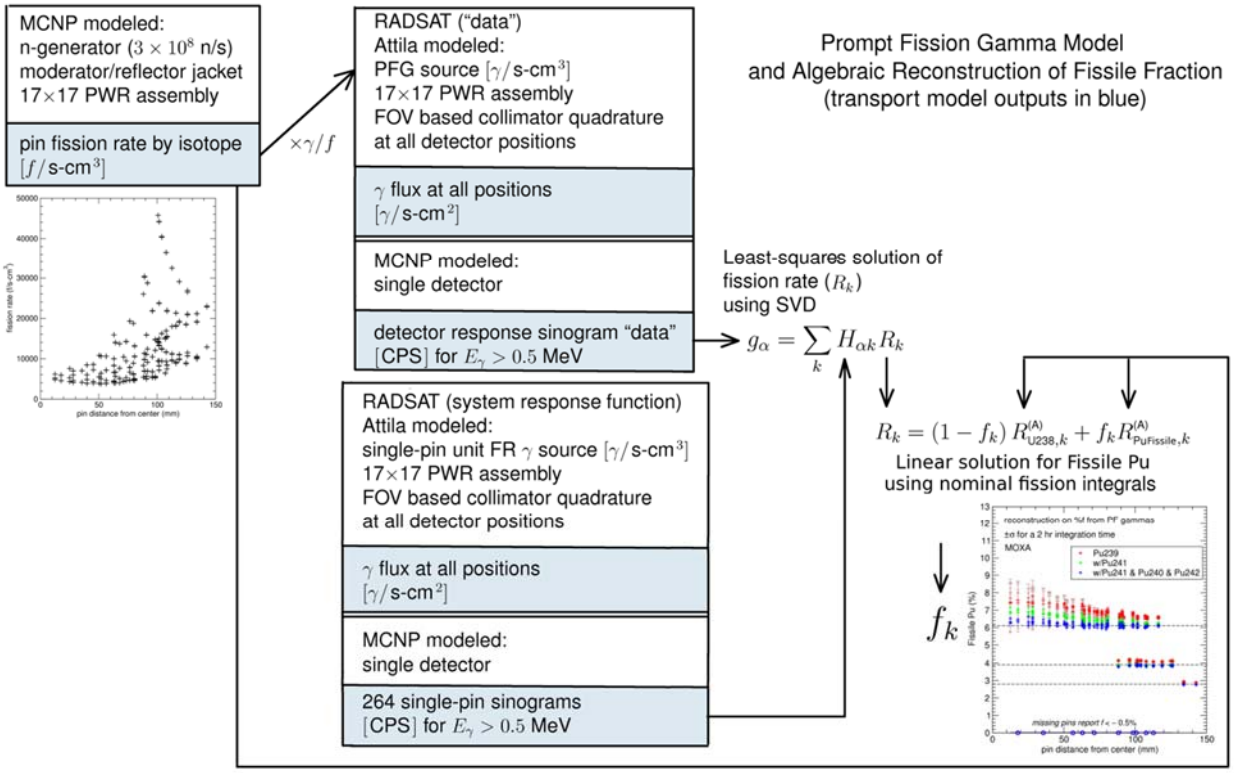

Figure 24. Overview of HGET performance-prediction methodology (assuming a PWR MOX assembly) that begins with forward calculations of induced fission rate (upper left) and culminates in quantification of fissile Pu concentration in each pin.

The HGET modeling and analysis framework depicted in Figure 23 was exercised on two different case studies in FY16, as reported below. In the performance prediction discussion and results presented below, the term "fissionable" is used to refer to the even-numbered isotopes that have no appreciable cross-section for thermal fission. "Fissile" refer to those isotopes for which the thermal cross-section is dominant. These definitions may be different than other authors employ, but are used here nonetheless.

7.1 Case Study 1: No Pu isotopic information

In this initial performance case study, the following approximations were made in its methods to translate reconstructed fission rate into pin-by-pin concentration of fissile Pu:

1. All fissionable isotopes (e.g., even-number Pu isotopes) can be approximated as ^{238}U;
2. The fission cross-sections of all odd-numbered Pu isotopes can be approximated by ^{239}Pu;
3. The spatial and energy dependence of the interrogating neutron flux inside any PWR MOX assembly can be approximated by the characteristics of MOXA;
4. Pu isotopics for the assembly are not known.

Shown in Figure 25 is the fission rate data corresponding to the first three assumptions above. There, the energy-dependent flux in each pin of the assembly is convolved (separately) with the cross-section for ^{239}Pu, ^{241}Pu and ^{238}U. The fission-rate integral for each isotope is plotted as a function of distance from the D-T interrogating source. Observations from that plot include that the fission rate pattern for ^{238}U can be represented by a $1/r^{1.5}$ fall-off relative to the neutron generator location and an exponential attenuation term. This relationship reflects the fact that ^{238}U fission is induced primarily by fast neutrons. In the HGET viability analysis presented in this report, it is assumed that this ^{238}U fission-integral behavior does not vary significantly across the range of typical PWR MOX characteristics (i.e., pin loadings) and therefore, that the pin-by-pin relationship between HGET interrogating neutron flux and ^{238}U fission integral for MOXA can be applied to all MOX variants.

The fission-integral patterns for ^{239}Pu and ^{241}Pu are decidedly different since fission is dominated by thermal and epithermal neutrons in those isotopes. The pattern for these isotopes reflects the fact that the fission rate in outer pins will be much higher than in the interior pins due to the effects of the HGET moderator/reflector on the perimeter and self-attenuation for the interior. The effect of the somewhat higher cross-section for thermal fission (~1010 barns for ^{241}Pu, ~750 barns for ^{239}Pu) is also evident—the ^{241}Pu fission integral is uniformly higher. In this first case study, the notable differences between the ^{239}Pu and ^{241}Pu fission integrals are ignored for simplicity and that the fission integral of ^{239}Pu can be taken to represent that of ^{241}Pu.

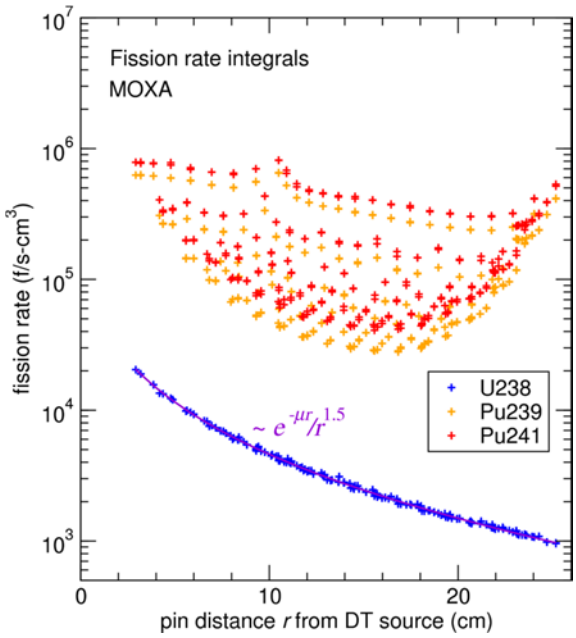

Figure 25. Fission-rate integrals for ^{238}U, ^{239}Pu and ^{241}Pu, for each pin in MOXA, as function of distance from the D-T source.

Under the approximations stated above, the isotope-specific fission rate integrals, R_{U238} and $R_{PuFissile,}$ (as shown in Figure 25), can be used to determine the Fissile Pu fraction f_k in each pin. Figure 26 shows preliminary results for determination of Fissile Pu fraction f_k in the MOXA and MOXB assemblies. The true fissile fractions of the pins for MOXA (Figure 26, left) and MOXB (Figure 26, right) are shown with the dashed lines. Note that the true fissile fractions shown in Figure 26 are not exactly the same as the total Pu fraction because not all the Pu is fissile (e.g. ^{242}Pu).

Observations and interpretation from Figure 26 are given here:

- The 11 missing pins are detected, as declared. In this analysis, any negative result for the concentration of Fissile Pu was taken as a missing pin and assigned a fissile percentage of zero on the plots.
- The calculated Fissile Pu concentration is consistently higher than the true value, for all pin locations and Pu loading level. In MOXA, this systematic bias ranges from a few percent for outer pins with lower loading to approximately 20% for center pins with higher Pu loading. The relative standard deviation (RSD) of the difference between the calculated and true values, across all 253 pins in the MOXA assembly, is 13.9%, inclusive of bias at 11.8% One significant contributor to this bias is the assumption that all fissile Pu is ^{239}Pu, when in fact approximately one quarter of the Pu is ^{241}Pu, which has a somewhat higher fission cross-section.
- The reason for a bias that increases for inner pins is not completely understood at this time, but a key factor is the hardening of the interrogating flux toward the interior of the assembly. This hardening may increase the contributions of ^{241}Pu and even the fissionable ^{240}Pu and ^{242}Pu, relative to ^{239}Pu.
- The positive bias is clearly higher for MOXB (RSD of 23.5% for the 253 pins, bias of 20.8%) than MOXA. As discussed above, the MOXB calculations assume the fission integrals from MOXA, even though the total Pu loading and Pu isotopics in the two assemblies are quite different.

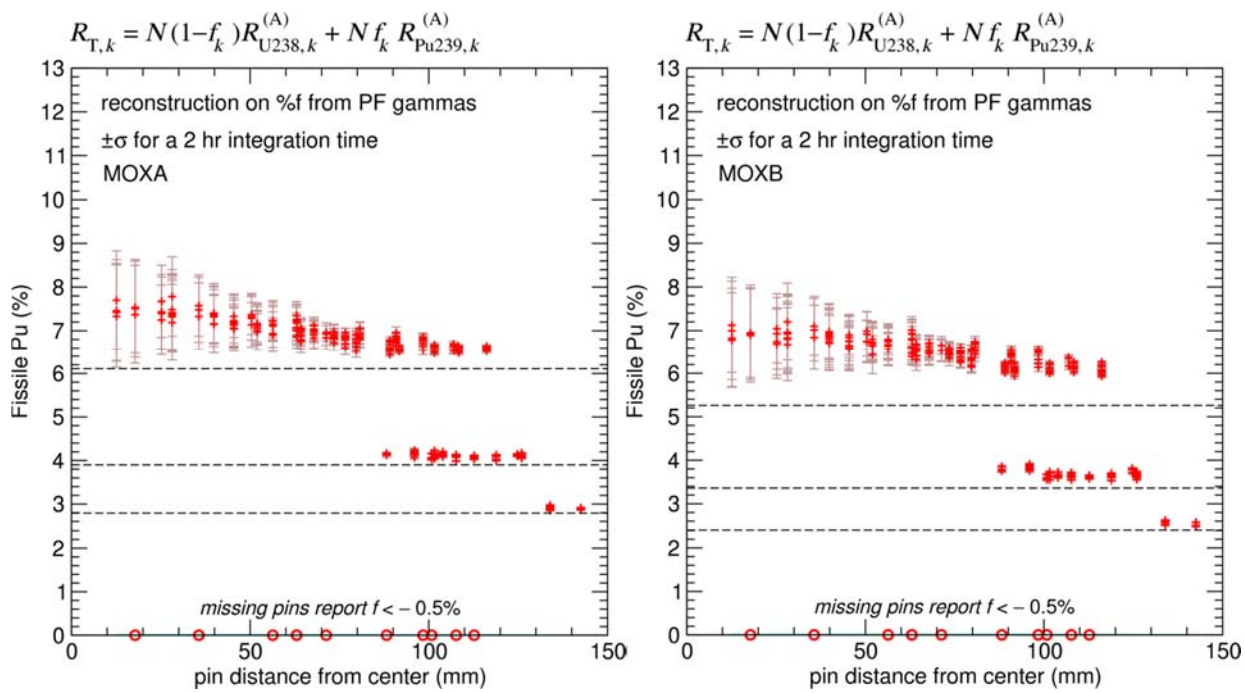

Figure 26. Initial results for the determination of Fissile Pu (^{239}Pu + ^{241}Pu) fraction using HGET for MOXA (left) and MOXB (right). Calculated values are based on 2-hour total assay time; one-sigma error bars on statistical uncertainty are shown. Dashed lines are the actual fissile fraction (^{239}Pu + ^{241}Pu) for the three Pu loading levels. (Note that Pu isotopics are identical for all loading levels within each assembly.)

The statistical uncertainties (one-sigma relative) are shown in Figure 25 for a 2 hour integration time. They range from negligible on the outer pins to approximately 10% on the inner pins. The average statistical uncertainty across all pins is 3.6% for MOXA and 3.8% for MOXB.

7.2 Case Study 2: Inclusion of Pu isotopic information

In Case Study 1, it was assumed that a ^{239}Pu fission integral accurately represents ^{241}Pu, and that the even-numbered fissionable (but not fissile) Pu isotopes make a negligible contribution to the induced fission rate. These assumptions were made for simplicity and also to set a baseline for the importance of data on Pu isotopics for HGET verification of MOX fuels. To explore how the fidelity of HGET verification might be improved by including known Pu isotopic information, either declared or directly measured by the IAEA, fission integrals for the other Pu isotopes were calculated (Figure 27, top) and progressively added into the analysis.

Figure 27 (bottom) shows that as the declared fractions of other Pu isotopes are added to the analysis, the accuracy of the Fissile Pu estimations is significantly improved. As expected, explicitly including the fissile ^{241}Pu (green markers) improves predictions in outer pins that have a largely well-moderated flux and; adding the fissionable isotopes improves the prediction of inner pins (blue markers), where the flux is somewhat hardened in comparison. Note that the ^{240}Pu and ^{242}Pu fission integrals were not independently evaluated but rather, for simplicity, approximated as the ^{238}U integral scaled by the magnitude of the induced fission cross-section for each isotope (i.e., 1.075 times ^{238}U).

The positive impact of including Pu isotopic information is clear: The RSD of the difference between calculated and true fissile fractions, across all pins, was 13.9% (bias of 11.8%) when all Pu was assumed to be ^{239}Pu, but this RSD fell to 1.95% with a positive bias of only 1.5% when declared/measured Pu isotopic data was incorporated.

As stated earlier, a key assumption in Figure 26 and Figure 27 is that the fission integrals of MOXA can be taken as representative of all PWR MOX assemblies of similar design and reasonably similar Pu loading levels. To test the soundness of this assumption, the results for verification of MOXB using MOXA integrals as normative, are given in Figure 28. The RSD of the difference between calculated and true fissile fractions, for all of the present pins, degrades for MOXB, as compared to MOXA. Assuming all declared/measured Pu isotopic data is incorporated (i.e., blue markers), the MOXB RSD is 7.80% for (including a bias of 6.7%), as compared to 1.95% for MOXA. The bias for verification of MOXB pins is significantly higher than for MOXA pins, particularly for pins at the highest loading, indicating a less-than-ideal model in the analysis process.

Though the bias in the MOXB pin-level values is significantly higher than for MOXA, it is worth noting that that precision of the pin-level values is largely the same. When taken in the context of the typical IAEA verification scenario, which focuses on identifying pins that are notably different than the declared values, this indicates that pins exhibiting fissile Pu fractions that diverge from its neighbors could still be faithfully detected, even if the absolute values for the assay of the neighbors have a bias.

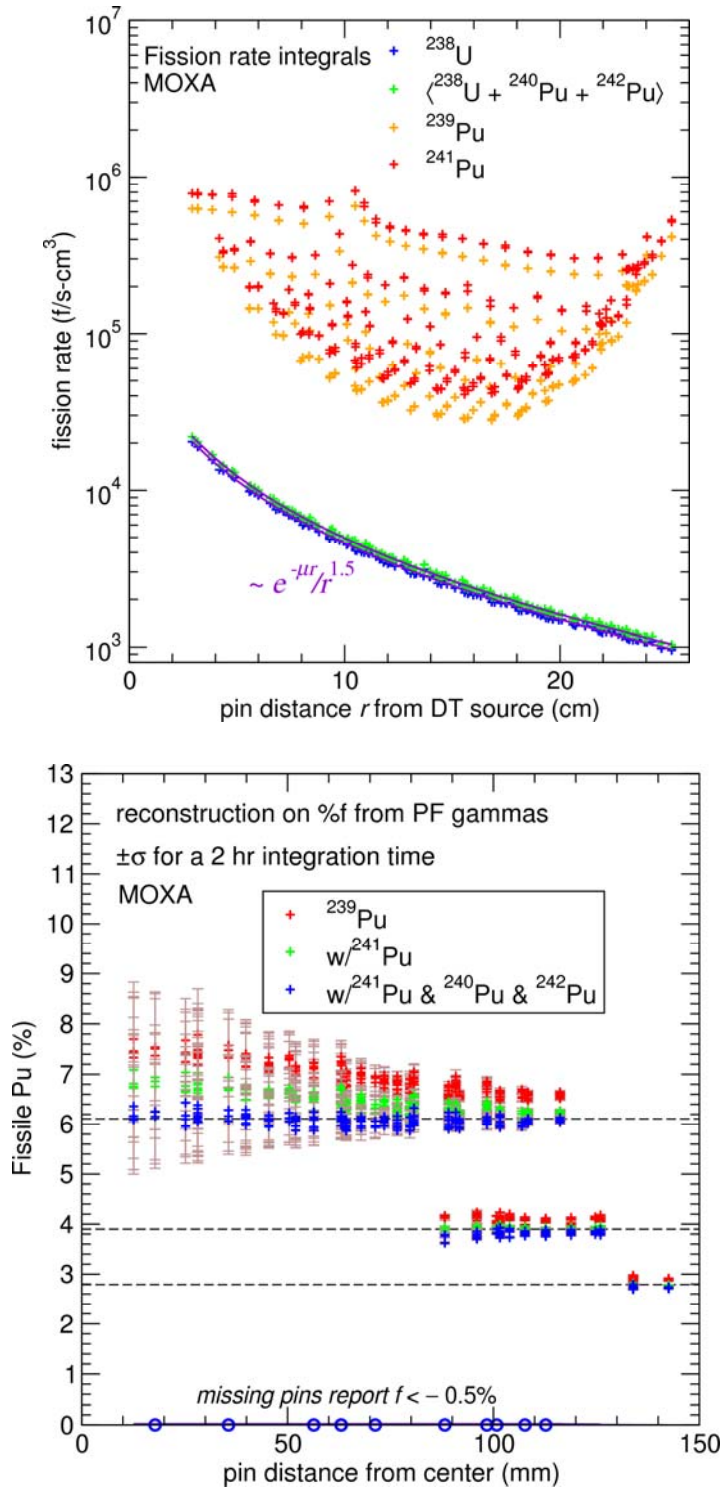

Figure 27. Top: fission-rate integrals for ^{238}U, ^{239}Pu, ^{240}Pu, ^{241}Pu and ^{242}Pu, for each pin in MOXA, as function of distance from the D-T source. Bottom: Initial results for the determination of Fissile Pu (^{239}Pu + ^{241}Pu) fraction in MOXA, when the incorporating Pu isotopics data in the analysis process. Calculated values are based on 2-hour total assay time; one-sigma error bars on statistical uncertainty are shown. Dashed lines are the actual fissile fraction (^{239}Pu + ^{241}Pu) for the three Pu loading levels. (Note that Pu isotopics are identical for all loading levels).

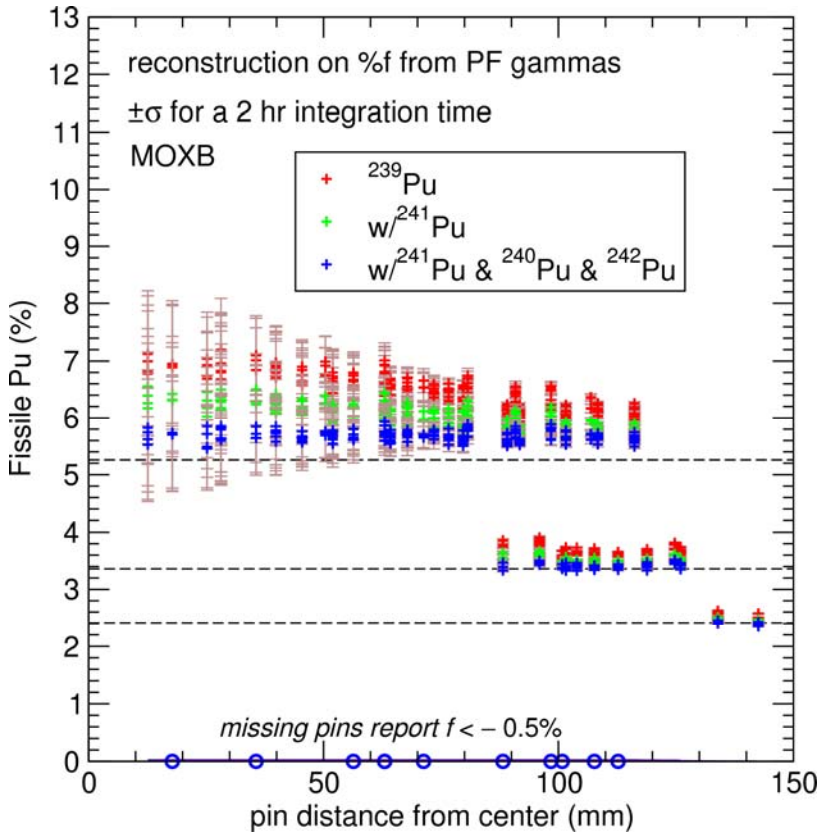

Figure 28. Initial results for the determination of Fissile Pu (^{239}Pu + ^{241}Pu) fraction in MOXB, using the fission integrals from MOXA. Calculated values are based on 2-hour total assay time; one-sigma error bars on statistical uncertainty are shown. Dashed lines are the actual fissile fraction (^{239}Pu + ^{241}Pu) for the three Pu loading levels. (Note that Pu isotopics are identical for all loading levels).

8.0 Summary and Next Steps

The HGET viability analysis presented in this report is based around the use cases and performance of the instrumentation that the IAEA currently uses for unirradiated fuels: the Uranium Neutron Coincidence Collar (UNCL) for fresh LEU fuels; Passive Neutron Coincidence Collar (PNCL) for MOX fuels. The International Target Values (ITVs) for these instruments are: 4.5% (one-sigma relative) for total ^{235}U mass in an LEU assembly using UNCL; 3.2% for total Pu mass in a MOX assembly using PNCL. Count times are not specified in the ITV document, but information provided by other sources indicate that measurement times can be as little as 15 minutes for PNCL but over 10 hours for UNCL on LEU fuels with heavy gadolinium loading. These ITVs for volume-averaging instruments provide useful context for the evaluation of new instruments, but it is important to note that that current ITVs do not exist for pin-level determination of fissile mass. *Verification at pin level, the goal of HGET assay, would be a completely new capability for the IAEA.*

A summary of the four major tasks undertaken in the FY16 HGET scope is presented below:

1. Candidate Signatures: Several candidate gamma-ray signatures, including prompt fission, delayed fission, prompt capture and purely passive were evaluated in terms of their intensity and specificity for quantification of fissile isotope concentration. The FY16 findings were that prompt-fission gamma rays, collected over broad energy regions (e.g., 0.5 MeV and above) offer the most promise, but delayed-fission gamma rays may also be useful as a complimentary signal. While the imaging of gamma rays over broad energy ranges (prompt-fission or delayed-fission) precludes imaging the concentration of individual fissile isotopes (e.g., ^{235}U or ^{239}Pu in an assembly), such a method can image the total-fissile concentration.
2. HGETv1 Design Study: Using the IAEA's PGET device as a foundational form factor (large arrays of collimated detectors; rotation only for acquisition of projections), various combinations of neutron generators and moderator/reflector geometries were evaluated with the goal of producing high thermal and epithermal neutron fluxes that preferentially induce fission in the fissile isotopes (as opposed to fast fission in the fissionable ^{238}U) with a spatial distribution that is as uniform as possible to prevent large gradients illumination across the assembly. Given the relatively weak neutron-induced gamma-ray signatures, an HGET instrument requires detector types and collimator designs that trade off spatial resolution in favor of higher collection efficiency.
3. Reconstruction and analysis algorithms: Standard tomographic reconstruction algorithms, for example those used in nuclear medicine and spent-fuel tomography, require high signal-to-noise in the raw signatures, and are hampered by the strong gradients in count rates between inner and outer pins. Since the HGET use case involves relatively weak signatures and high gradients across the assembly due in large part to the coupling of neutron and gamma-ray self-shielding, there is a need to develop new reconstruction algorithms specific to HGET and the ultimate goal of IAEA measurements (i.e., confirmation of an operator's declaration about the assembly, as opposed to assay of the assembly as a completely unknown object). The project preliminarily investigated several potential algorithms, and work on that front continues. In the performance prediction study of FY16, a relatively simple algebraic reconstruction technique was employed, based on least-squares analysis and singular value decomposition, to calculate the fission rate in each pin of the assembly. The fission rate was then translated to fissile-isotope concentration using a novel method to de-tangle the portion of the fission rate due to fast fission in the ever-present ^{238}U, and the thermal/epithermal fission in the fissile isotopes of interest such as ^{239}Pu, ^{241}Pu, ^{235}U.

4. Performance Prediction: A modeling and analysis framework was developed to perform forward calculations of HGET response to representative assemblies, and perform the inverse problem to solve for pin-level fissile isotope concentration. This framework was exercised for MOX assemblies, assuming the prompt fission-gamma signature, using a set of assumptions regarding the IAEA use case and verification scenario, and simplifying approximations in the analysis stages.

The performance predictions in this report are predicated on the goal of determining whether there are any inconsistencies between the operator's declaration of the assembly, and the reconstructed pin-wise results (e.g., fissile Pu in a pin location where none was declared, or vice versa). This analysis concept is consistent with the IAEA concept of verification, but is to be distinguished from the challenge of "blind assay". These algorithms could also be used as part of an iterative process, where an initial model-independent reconstruction (such as filtered backprojection) is performed to verify assembly type (e.g., PWR 17x17), and then subsequent calculations use the stated assembly geometry.

The preliminary findings from this first year of study indicate that: given a careful system design, a COTS portable neutron generator and reconstruction and analysis algorithms that fully acknowledge operator-declared information about the assembly, HGET has the potential to verify fissile-mass concentration on a pin-by-pin basis in total assay times of approximately 2 hours for a representative PWR MOX assembly. These initial performance estimates assumed that assembly type, missing-pin locations and Pu isotopics were accurately declared by the operator and incorporated in the analysis process. Under those assumptions, the average statistical precision across the 253 pins was approximately 3.6%, varying from less than 1% (one-sigma relative) for pins at the perimeter of the assembly, where the induced signal is most easily collected, to approximately 10% for the most inner pins, where the interrogating neutron flux and the induced prompt gamma-ray signatures undergo more attenuation. The relative standard deviation of the fissile-Pu quantification, over all 253 pins, was less than 2% of which approximately 1.5% was a positive bias. This bias was small compared to the reconstructed contrast for missing pins--missing pins were clearly distinguishable from present pins. While these initial performance estimates are quite encouraging, there are a number of assumptions and caveats that need to be addressed in order to more fully understand their impact on expected HGET performance.

The FY16 HGET study provides a solid foundation on which to build in FY17. Recommended scope in FY17 is summarized here:

- Extend the feasibility analysis to LEU, and to LEU with burnable poisons (Gd rods). The case of Gd loading in particular is challenging for coincidence counting assay, and is of particular interest.
- Reconstruction methods: FY16 analysis has shown that algorithms incorporating detector response and pin-wise attenuation can improve defect-detection and isotopic quantification considerably, but simultaneously determining attenuation and activity is difficult. Innovative algorithms are needed; examples include the use of multiple energy windows in the projection data to infer spatial attenuation, and iterative maximum-likelihood approaches. The robustness of HGET reconstruction methods to imperfections in the system response function (e.g., undeclared or inaccurately declared missing pins) will be a focus of FY17 analysis. It is also important to increase the level of independence between the forward calculations used to simulate HGET response, and the transport calculations used to generate the system response function. (In FY16, both were performed using RADSAT.)

- Other signatures: In FY16, performance predictions were performed using only the prompt-gamma signature. Delayed gamma counts become significant as the measurement progresses, and should be included in the reconstruction algorithms as a smoothly varying time dependent term.
- Increased doses of reality: For simplicity in modeling, the HGETv1a design used in FY16 assumes an idealized arrangement of the moderator/reflector and detector arrays that cannot be achieved in practice. The HGET modeling framework needs to be modified to more accurately reflect the likely realities of IAEA implementation. Also, all FY16 scoping analysis assumed a negligible background during HGET assay. An investigation of background source terms should be undertaken, via simulation and laboratory measurements, and incorporated in the modeling and analysis framework in order to more faithfully capture their effects. To date, the effect of gadolinium loading has not been considered, but needs to be in order to provide meaningful comparisons to the UNCL and the associated challenges with high-Gd fuels. Perhaps most importantly, the HGET viability study needs to move into empirical space. The challenges of high-fidelity simulation for this relatively complex active interrogation approach (for which even basic cross-section data are not always available) strongly encourage proof-of-principle laboratory measurements using a representative tomographic device and objects (e.g., LEU fuel rodlets), to benchmark the predictive modeling tools and guide refinement of the nominal HGET instrument design. Preliminary work to develop an emission tomography test bed, under funding from both internal PNNL resources and NA-241 Safeguards Technology, is described in Appendix A.

9.0 References

1. *IAEA Department of Safeguards Long-Term R&D Plan, 2012-2023*. 2013, IAEA: Vienna, Austria.

2. Svard, S.J., et al., *Gamma-ray Emission Tomography: Modeling and Evaluation of Partial-Defect Testing Capabilities*, in *2014 IAEA Symposium on International Safeguards*. 2014.

3. Smith, L.E., et al., *A Viability Study of Gamma Emission Tomography for Spent Fuel Verification: JNT 1955 Phase I Technical Report*. 2016, Pacific Northwest National Laboratory: Richland, WA. p. 197.

4. Campbell, L.W., L.E. Smith, and A.C. Misner, *High-Energy Delayed Gamma Spectroscopy for Spent Nuclear Fuel ASsays.* IEEE Transactions on Nuclear Science, 2011. **58**(1).

5. Mozin, V., et al., *Delayed gamma-ray spectroscopy for spent nuclear fuel assay.* Journal of Nuclear Materials Management, 2012. **40**(3): p. 78-87.

6. *Safeguards Techniques and Equipment: 2011 Edition*, in *International Nuclear Verification Series*. 2011: Vienna, Austria. p. 162.

7. Zhao, M., et al., *International Target Values 2010 for Measurement Uncertainties in Safeguarding Nuclear Materials.* ESARDA Bulletin, 2012. **48**: p. 3-24.

8. Canberra Industries, I. 2011 [cited 2016 December 1]; Available from: http://www.canberra.com/products/waste_safeguard_systems/pdf/JCC-71-72-73-SS-C38898.pdf.

9. Bairiot, H., et al., *Status and Advances in MOX Fuel Technology*, in *Technical Reports Series*. 2005, International Atomic Energy Agency: Vienna, Austria. p. 179.

10. Verbinski, V.V., H. Weber, and R.E. Sund, *Prompt Gamma Rays from from 235U(n,f), 239Pu(n,f), and Spontaneous Fission of 252Cf.* Physical Review C, 1973. **7**(3): p. 1173-1185.

11. Mozin, V.V., S.J. Tobin, and J. Vujic, *Delayed Gamma Instrument for Determining Plutonium Mass in Spent Nuclear Fuel.* Transactions of the American Nuclear Society, 2010. **102**: p. 456-7.

12. Campbell, L.W., L.E. Smith, and A.C. Misner, *High-Energy Delayed Gamma Spectroscopy for Spent Nuclear Fuel Assay.* Ieee Transactions on Nuclear Science, 2011. **58**(1): p. 231-240.

13. Mozin, V., et al., *Delayed Gamma-Ray Spectroscopy for Non-Destructive Assay of Nuclear Materials*. 2015, Lawrence Livermore National Laboratory: Livermore, CA.

14. *International Atomic Energy Agency PGAA Database*.

15. *Evaluated Nuclear Data File (ENDF/B-VII.1) Library*.

16. Campbell, L., *Fitting Methods for Delayed Gamma Spectroscopic Data*. 2013, Pacific Northwest National Laboratory: Richland, WA.

17. Pelowitz, D., (editor), *MCNP6™ User's Manual*. 2011, Los Alamos National Laboratory: Los Alamos, NM.

18. Wilson, W.B., et al., *A Manual for CINDER'90 Version 07.4 Codes and Data*. 2008, Los Alamos National Laboratory: Los Alamos, NM.

19. Mozin, V. and S.J. Tobin, *DGSDEF: Discrete Gamma-ray Source DEFinition Code*. 2010, Los Alamos National Laboratory: Los Alamos, NM.

20. Wareing, T.A., J.M. McGhee, and J.E. Morel, *ATTILA: A Three-Dimensional, Unstructured Tetrahedral Mesh Discrete Ordinates Transport Code.* Transactions of the American Nuclear Society, 1996. **75**.

21. Smith, L.E., et al., *Coupling Deterministic and Monte Carlo Transport Methods for the Simulation of Gamma-Ray Spectroscopy Scenarios.* Ieee Transactions on Nuclear Science, 2008. **55**(5): p. 2598-2606.

22. *Emission Tomography: The Fundamentals of PET and SPECT*. 1 ed. 2004: Elsevier Academic Press. 576.

23. Rezaei, A., et al., *Simultaneous Reconstruction of Activity and Attenuation in Time-of-Flight PET.* IEEE Transactions on Medical Imaging, 2012. **31**(12).

Appendix A

Emission Tomography Test Bed

Appendix A

Emission Tomography Test Bed

Modeling emission tomography can give the first indications of feasibility for new methods, but ultimately measurements are needed to gauge performance. Here, a single pixel emission tomography test bed is presented. This system was developed under a mix of funding, including internal PNNL investment, NA-241 Human Capital Development funding to work with a team of mechanical engineering students from Washington State University for the frame design and construction, and NA-241 Safeguards Technology funding for the HGET project.

A.1 Experimental Setup and Initial Measurements

The single pixel emission tomography test bed uses a single collimated detector translated along a line to collect data equivalent to a bank of collimated detectors such as with the PGET instrument or the conceptual HGET design. This allows for testing emission tomography concepts at relatively low system cost, but at the expense of increased measurement time. The emission test bed, pictured in Figure A.1, was constructed using a rotation stage with a 380 mm diameter center aperture (Intellidrives, Inc. RTLA-380-560 with a servo drive) which can rotate over 360 degrees. A linear stage with 391 mm travel (Newport IMS400CC), enough to fully span the field of view, is mounted on top of the rotary stage. A 3 in x 3 in NaI detector coupled to an Osprey base is mounted on the linear stage, surrounded by 1.27 cm thick lead shielding. A lead collimator is placed in front of the detector, with a length of 5.08 cm, and an aperture that is 0.3 cm x 5.08 cm (Figure A.2).

Figure A.1. Photograph of the GET laboratory test bed developed through a combination of PNNL internal resources and NA-241 funding.

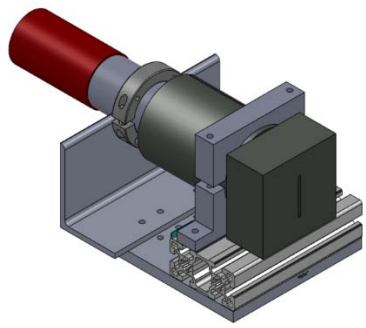

Figure A.2. A CAD drawing of the NaI detector, lead collimator block, lead collar, and corresponding holder that is mounted on the linear stage.

A simple emission tomography measurement was taken, using two button test sources, ^{137}Cs(8 μCi) and ^{57}Co (3.2 μCi). The following parameters were used:

Linear start position: 7.8 mm
Linear increment: 18.4 mm
Linear N increment (number of steps taken): 21
Rotary degree Increment: 10.2

This resulted in 21 energy spectra being collected, in 18.4 mm increments, at each of the 37 projection angles. The corresponding sinograms for this measurement were evaluated using filtered backprojection.

A.2 Preliminary Empirical Results

The two-source measurement, consisting of a ^{137}Cs and a ^{57}Co button source, took approximately 13 hours to acquire 21-one minute energy spectra, collected 18.4 mm apart from one another, at 37 different projection angles about the rotating stage. Figure A.3 represents the resulting sinograms generated from the 32 keV peak (^{137}Cs), 662 keV peak (^{137}Cs), 122 keV peak (^{57}Co), and all three peaks combined.

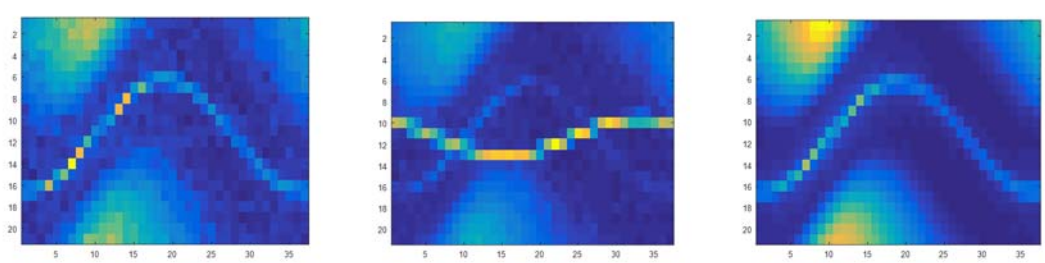

Figure A.3. The sinogram generated from the 32 keV peak from ^{137}Cs; 122 keV peak from ^{57}Co; 662 keV peak from ^{137}Cs.

These sinograms were then used to generate two sets of reconstructed images, the first set being the reconstruction of each source independently (Figure A.4), then a composite image that merges the sinograms of all three sources (Figure A.5).

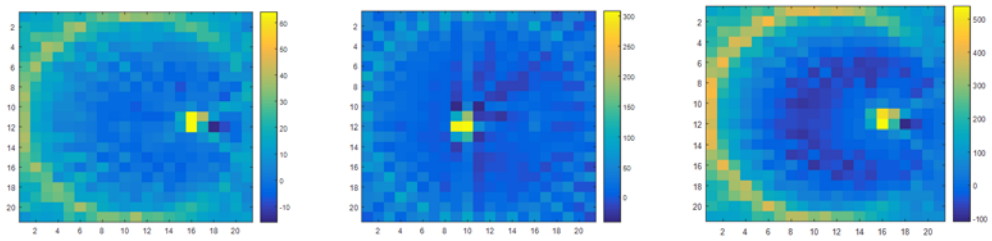

Figure A.4. Images generated from the individual sinograms in Figure A.3 using filtered backprojection.

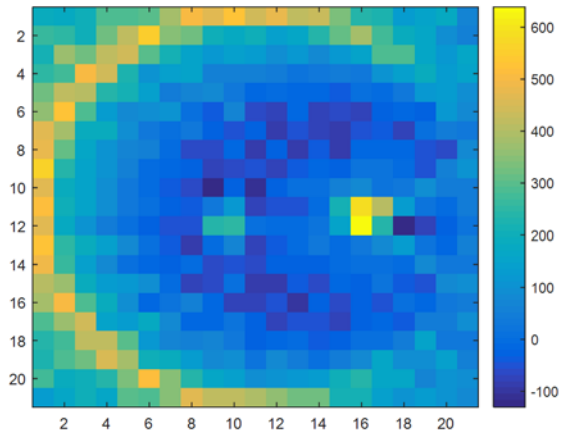

Figure A.5. Image generated from the aggregation of sinograms from Figure A.3 using filtered backprojection.

In the combined back projection image, one can clearly resolve both sources and see that the ^{137}Cs (8 μCi) source has a higher activity than the ^{57}Co (3.2 μCi) source. A ring shaped artifact can be seen in the reconstructed images. This is due to penetration through the ½ " thick lead collar (Figure A.2) surrounding the NaI detector. In particular, the collimator block that was placed in front of the detector is 2" thick, while the lead collar is only ½" thick, meaning as the detector translates closer to the end of the linear track, the incident gammas are attenuated less, and therefore more are able to interact with the detector. This is apparent when comparing the 662 keV image to the 32 keV, where this "ring" is more intense.

The measurements and initial reconstruction results presented above are proof-of-principle in nature, largely to demonstrate the readiness of the PNNL tomography test bed for future empirical work. Future measurements should be taken with different sources (i.e. size, shape, activity, etc.) and different system parameters, such as different detector types, linear increments, rotatory degree increments, etc. In addition, further investigation into the current and future test source holders, will help improve current benchmarking and alignment protocols.

www.pnnl.gov

Pacific Northwest
NATIONAL LABORATORY

Proudly Operated by **Battelle** *Since 1965*

U.S. DEPARTMENT OF
ENERGY

902 Battelle Boulevard
P.O. Box 999
Richland, WA 99352
1-888-375-PNNL (7665)